



HAL
open science

Petrogenetic implications of chromite-seeded boninite crystallization experiments: Providing a basis for chromite-melt diffusion chronometry in an oxybarometric context

Daniel A. Coulthard Jr, Georg F. Zellmer, Akihiko Tomiya, Sébastien Jégo,
Raimundo Brahm

► To cite this version:

Daniel A. Coulthard Jr, Georg F. Zellmer, Akihiko Tomiya, Sébastien Jégo, Raimundo Brahm. Petrogenetic implications of chromite-seeded boninite crystallization experiments: Providing a basis for chromite-melt diffusion chronometry in an oxybarometric context. *Geochimica et Cosmochimica Acta*, 2021, 297, pp.179-202. 10.1016/j.gca.2021.01.017. insu-03123506

HAL Id: insu-03123506

<https://insu.hal.science/insu-03123506>

Submitted on 28 Jan 2021

HAL is a multi-disciplinary open access archive for the deposit and dissemination of scientific research documents, whether they are published or not. The documents may come from teaching and research institutions in France or abroad, or from public or private research centers.

L'archive ouverte pluridisciplinaire **HAL**, est destinée au dépôt et à la diffusion de documents scientifiques de niveau recherche, publiés ou non, émanant des établissements d'enseignement et de recherche français ou étrangers, des laboratoires publics ou privés.

Journal Pre-proofs

Petrogenetic implications of chromite-seeded boninite crystallization experiments: Providing a basis for chromite-melt diffusion chronometry in an oxybarometric context

Daniel A. Coulthard Jr, Georg F. Zellmer, Akihiko Tomiya, Sébastien Jégo, Raimundo Brahm

PII: S0016-7037(21)00039-9
DOI: <https://doi.org/10.1016/j.gca.2021.01.017>
Reference: GCA 12047

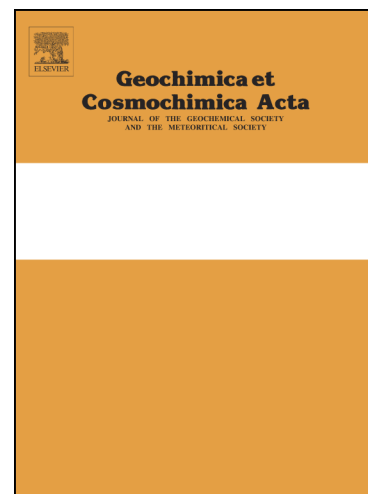
To appear in: *Geochimica et Cosmochimica Acta*

Received Date: 12 August 2020
Revised Date: 13 January 2021
Accepted Date: 18 January 2021

Please cite this article as: Coulthard, D.A. Jr, Zellmer, G.F., Tomiya, A., Jégo, S., Brahm, R., Petrogenetic implications of chromite-seeded boninite crystallization experiments: Providing a basis for chromite-melt diffusion chronometry in an oxybarometric context, *Geochimica et Cosmochimica Acta* (2021), doi: <https://doi.org/10.1016/j.gca.2021.01.017>

This is a PDF file of an article that has undergone enhancements after acceptance, such as the addition of a cover page and metadata, and formatting for readability, but it is not yet the definitive version of record. This version will undergo additional copyediting, typesetting and review before it is published in its final form, but we are providing this version to give early visibility of the article. Please note that, during the production process, errors may be discovered which could affect the content, and all legal disclaimers that apply to the journal pertain.

© 2021 Elsevier Ltd. All rights reserved.



1
2
3
4
5
6
7
8
9
10
11
12
13
14
15
16
17
18
19

Petrogenetic implications of chromite-seeded boninite crystallization experiments:

Providing a basis for chromite-melt diffusion chronometry in an oxybarometric context

¹*Daniel A. Coulthard Jr., ¹Georg F. Zellmer, ²Akihiko Tomiya, ³Sébastien Jégo, ¹Raimundo Brahm

¹Volcanic Risk Solutions, School of Agriculture and Environment, Massey University, Private Bag 11 222, 4414 Palmerston North, New Zealand; g.f.zellmer@massey.ac.nz, r.brahm@massey.ac.nz

²Geological Survey of Japan, Advanced Institute of Science and Technology Tsukuba Central 7, 1-1-1 Higashi, Tsukuba, Ibaraki 305-8567, Japan; a.tomiya@aist.go.jp

³Institut des Sciences de la Terre d'Orléans, UMR 7327, CNRS/INSU-Université d'Orléans-BRGM, 1A rue de la Férellerie, 45071 Orléans, France; s_jego@hotmail.com

*Corresponding author: d.a.coulthard@massey.ac.nz, phone: +64 21 168 1669

Keywords: Experimental Petrology, Internally Heated Pressure Vessel, Magma Ascent, Timescales, Crystal-Melt Disequilibrium,

ABSTRACT

20 Boninites are rare high magnesium andesites that often contain trace chromites. These
21 chromites precipitate from primitive boninitic melts and are thought to be carried to the
22 surface in melts that continue to crystallize a significant volume of silicate minerals. Such
23 magmatic differentiation drives primitive chromite out of equilibrium with the residual melt
24 with respect to both divalent and trivalent cation proportions. Diffusion then operates to alter
25 primitive chromite toward a composition in equilibrium with residual melt. To simulate this
26 process, we have performed internally heated pressure vessel experiments, providing insights
27 into the processes of chromite-melt re-equilibration through time. While Fe-Mg exchange at
28 magmatic temperatures equilibrates the tetrahedrally coordinated divalent cations in chromite
29 in less than 6 hours, equilibration of trivalent cations in octahedral coordination with residual
30 melts is slower. Our experimental results show that chromite Al concentrations are
31 ubiquitously lower, and $\text{Fe}^{2+}/\text{Fe}^{3+}$ values are ubiquitously higher than modelled equilibrium
32 values, indicating that there was insufficient time for significant Al and Fe^{3+} replacement of
33 Cr. Similar observations can be made for natural chromite compositions in the extrusive
34 sequence of the Troodos ophiolite (Cyprus). Based on a simple model of diffusive
35 equilibration, we estimate that microphenocrystic chromites up to 60 μm in diameter take
36 between 60 days and *c.* 170 years to equilibrate under conditions analogous to the
37 physiochemical state of melt immediately prior to eruption. For the Troodos ophiolite
38 extrusive sequence, this implies that mafic magmas are erupted less than *c.* 170 years after
39 extraction from the mantle for disequilibrium textures and compositions to be preserved.

40 1. INTRODUCTION

41 Boninites are rare high magnesium andesites that are produced by the melting of highly
42 depleted mantle (harzburgite) under shallow and hydrous conditions (Pearce and Reagan,
43 2019). The paucity of this rock type in the geologic record may be attributed to the exotic

44 nature of these petrogenetic conditions and/or the tendency of boninites to erupt in places
45 with a low preservation potential (e.g. forearc regions, Stern and Bloomer, 1992).
46 Nevertheless, boninites are generated in several tectonic settings including intraoceanic arcs
47 (Meijer, 1980), intracontinental arcs (Tatsumi, 2006), back-arc basins (Falloon et al., 1992),
48 and oceanic plateaus (Golowin et al., 2017). Additionally, several boninites have been found
49 in ophiolite terranes (e.g. Bédard, 1999; Cameron, 1985; Dilek and Thy, 2009; Ishikawa et
50 al., 2002; Meffre et al., 1996), though the tectonic settings of some ophiolites are topics of
51 rigorous debate (cf. Gass, 1968; Metcalf and Shervais, 2008; Miyashiro, 1973; Moores et al.,
52 2000; Pearce and Robinson, 2010; Regelous et al., 2014; Woelki et al., 2020; Woelki et al.,
53 2018).

54 A cogenetic relationship between boninitic melt and podiform chromitite deposits found in
55 some ophiolitic mantle sections has been hypothesized (Arai, 1997; Arai and Yurimoto,
56 1994, 1995; Rollinson, 2008; Rollinson et al., 2018; Zhou and Robinson, 1997; Zhou et al.,
57 1994). With regard to podiform chromitite formation, it has been suggested that primitive
58 hydrous melts react with depleted mantle, become silica-enriched via the incongruent melting
59 of orthopyroxene (implying olivine crystallization), and crystallize a large volume of high-
60 Cr# chromite due to change in the number of available melt octahedral sites (Edwards et al.,
61 2000). Separately, mechanisms of chromitite formation have been experimentally explored
62 assuming immiscibility between melt-melt or melt-fluid components (Ballhaus, 1998;
63 Matveev and Ballhaus, 2002). Initial immiscibility has been observed in other experimental
64 studies that focused on the formation of boninitic melts via the same petrogenetic mechanism
65 (i.e. incongruent melting, Fisk, 1986), and the boninitic composition of melts are preserved in
66 equilibrium experiments that simulate melt-peridotite reactions (Mitchell and Grove, 2016). It
67 is noteworthy that one experiment (C608) of Mitchell and Grove (2016) not only produced
68 boninite melt in equilibrium with a dunite residual mantle mineral assemblage, but that the

69 composition of the residual mineral assemblage overlaps with the most depleted end of the
70 olivine-spinel mantle array in compositional space (Arai, 1994). Ultimately, few studies have
71 explicitly attempted to reconcile the links between boninite magma genesis, chromitite
72 formation, and/or, more generally, chromite crystallization (Arai, 1997; Arai and Yurimoto,
73 1994, 1995; Rollinson, 2008; Rollinson et al., 2018; Zhou et al., 1994; Zhou et al., 1996).

74 If boninitic melts are generated during concomitant olivine and chromite precipitation as
75 described above, then the appearance of high-Cr# chromite (and forsteritic olivine) in
76 boninites may be due to their removal from a mantle domain rather than crystallization from
77 extracted melts in the crustal domain, where chromite has not been observed to crystallize
78 under experimental conditions analogous to those that are realistic for primitive melt
79 differentiation (e.g. pressures > 1 bar, Umino and Kushiro, 1989).

80 It is important to specify the full implications of this model of boninite + chromitite
81 petrogenesis, namely that boninite and chromitite appear to be linked by a cogenetic
82 relationship based on observations of each in ophiolitic assemblages, that the underlying
83 relationship is essentially a reactive transport process that occurs in the shallow subarc
84 mantle, and that information on such processes may be inferred by detailed studies of
85 chromite-melt or chromite-olivine-melt geochemistry; the systematics of which are preserved
86 to different degrees in natural volcanic and plutonic suites (e.g. Kamenetsky et al., 2001).
87 Further, if chromites are plucked from the melt-mantle petrogenetic system, then their melt
88 inclusions (e.g. Kamenetsky et al., 2002; Umino et al., 2018; Umino et al., 2015) may give
89 valuable information regarding the nature of magma genesis in the reactive transport regime.

90 In the present study, we conducted a series of high-pressure (*c.* 2 kbar) experiments to create
91 systems wherein high silica boninite crystallized over brief time periods in the presence of
92 stable chromite. The data presented here demonstrate that chromite is little affected by

93 crystallization processes over short timescales unless unrealistically oxidizing conditions are
94 imposed. Silicate mineral assemblages form via equilibrium crystallization in hydrous melts
95 without significantly altering chromite compositions save for Mg-Fe exchange when buffered
96 near the nickel-nickel oxide (NNO) buffer. We propose that the systems represented by these
97 experiments may be regarded as approximations of what occurs in natural chromite-bearing
98 primary melts during their crustal differentiation (Scowen et al., 1991). Similar observations
99 on partial chromite-melt equilibration in natural samples from the Troodos ophiolite (Cyprus)
100 allow a coarse quantification of the extraction time for the mafic magmas of the extrusive
101 suite, but more detailed diffusion chronometry on the chemical zonation patterns of natural
102 chromites will be required to provide tight constraints.

103 **2. MATERIALS AND EXPERIMENTAL METHODS**

104 Crystallization experiments were performed using internally heated pressure vessels (IHPVs)
105 at the Institut des Sciences de la Terre d'Orléans (ISTO), Université d'Orléans, France, as
106 well as at the Geological Survey of Japan (GSJ) in Tsukuba, Japan. Additional sample
107 preparation took place at ISTO and at the Japan Agency for Marine-Earth Science and
108 Technology (JAMSTEC) in Yokosuka, Japan.

109 *2.1. Starting materials*

110 Table 1 provides major element data for the starting materials as well as the bulk composition
111 of the mixture used for the experiments. Analyses of the starting materials are given
112 alongside sample data in the supplemental Tables S1 and S2. A fragment of high-Si boninite
113 taken via dredging from the Mariana forearc (sample YK0612 974-R6, Reagan et al., 2010)
114 was chosen as a suitable starting material based on observed chromite phenocrysts and
115 microphenocrysts in thin section, which indicated chromite stability. The fragment was
116 powdered and fluxed to form glass, which was analysed during our routine spectrometric

117 analysis (BO-G, Table S1) and re-powdered for sample loading. Chromite seeds sourced
118 from the mantle section of the Troodos Ophiolite were added to glass powders with the intent
119 of fostering further growth of chromite from boninitic melts. These seeds are unzoned and are
120 homogeneous (avg. Mg# = 62, Cr/[Al+Cr+Fe³⁺] = 70). Two sample mixtures were made by
121 mixing powdered glass with one size fraction of chromite (either >160 μm or < 32 μm in
122 size), and each starting mixture contained 2% added chromite (by mass). The size of the
123 seeds added to powdered glass were initially varied in order to test if seed size affects the
124 resultant modal mineralogy of the sample.

125 Nominally pure platinum capsules were used as sample containers. Sample mixtures were
126 first loaded and then hydrated with heavy water (²H₂O) using a microsyringe before the
127 capsules were welded shut. Each capsule contained *c.* 1 wt% ²H₂O prior to welding (Table 2).
128 ²H₂O was used instead of ¹H₂O to allow future analysis of water using secondary ion mass
129 spectrometry, with this substitution enabling easy distinction between added water and
130 background hydrogen. The quality of the welds was checked by immersing each capsule in
131 hot oil. All capsules were adequately sealed (poor welds emit a bubble stream, indicating an
132 inadequate seal).

133 NiO+NiPd redox sensors added to each experiment allowed for the hydrogen fugacity (f_{H_2})
134 imposed by the IHPV pressure medium to be evaluated, as redox sensors accurately reflect
135 the oxygen fugacity (f_{O_2}) imposed by the gas buffer (Pownceby and O'Neill, 1994; Taylor et
136 al., 1992). These sensors were made by packing two pellets into inert ZrO₂ powder within a
137 platinum capsule so that the pellets are not in contact with the capsule wall. One pellet was
138 made of 50% NiO and 50% Ni_xPd_{1-x} and the other was made of 50% NiO and 50% Ni_yPd_{1-y},
139 with $x = 0.5$ and $y = 0.85$. Deionized water was added until the capsule interior became

140 visibly saturated. Then the capsule was welded shut. Welds were checked in the same way
141 for the sensors as they were for the sample capsules.

142 2.2. *Experimental design*

143 The IHPVs used at ISTO and GSJ both employed molybdenum furnaces to perform the high
144 temperature experiments described here. Since the same amount of water was initialized in
145 each sample, by varying the temperature of the experiments between 1200, 1150, and 1100°C,
146 variable degrees of crystallinity are achieved in each sample. This determines the
147 concentration of water in residual melts, as the crystallization of nominally anhydrous mafic
148 minerals enriches the melt volume in incompatible volatile elements. The experiments were
149 performed under isobaric conditions, which means the final variable to consider is the fO_2 of
150 the system.

151 Target oxygen fugacities were *c.* 1-3 log units above the NNO buffer, which are analogous to
152 magmas generated in subduction zone settings (Brandon and Draper, 1996; Evans et al.,
153 2012; Kelley and Cottrell, 2009; Parkinson and Arculus, 1999). The oxidation states were
154 either left unbuffered or buffered by pressurizing the IHPV with an Ar-H₂ gas mixture
155 (pH_2^{added} , Table 2). Pt capsules are permeable to hydrogen, which diffuses through the
156 capsule wall to bond with oxygen in the melt so that reduction of the sample volume occurs
157 (Chou et al., 1978; Shaw, 1963). Since the volume of the pressure medium is much greater
158 than the volume of the sample capsule, the pressure medium is effectively an infinite
159 reservoir with respect to hydrogen. Thus, the effective concentration of hydrogen available to
160 each capsule during a given experiment, fH_2 , may be considered constant. Unbuffered
161 experiments cause the redox state of melts to approach a condition known as the intrinsic fO_2
162 of the IHPV. The intrinsic fO_2 of IHPV systems is highly oxidizing (NNO+2 to NNO+4,
163 Scaillet et al., 1992; Taylor et al., 1992, see further discussion in Supplemental Text 1).

164 The experiments described here each lasted less than 6 hours. The utility of short-period
165 experiments is multifaceted. From a volcanological perspective, fast ascending magmas are
166 extracted from their crustal domains and extruded onto the surface in as little as tens of
167 minutes (Lloyd et al., 2016) when melts are hot ($>1000^{\circ}\text{C}$) and volatile rich. Short timescales
168 of the order of hours to days have also been inferred for volatile poor arc magmas (Lormand
169 et al., 2020). In a rapidly ascending melt, a variety of concomitant processes may alter the
170 physiochemical state of the melt volume, including syn-eruptive mixing (e.g. Tomiya et al.,
171 2013; Wolf and Eichelberger, 1997), crystallization (e.g. Blundy and Cashman, 2005;
172 Cashman and Blundy, 2000), and whole-rock contamination (e.g. Mattioli et al., 2006). Such
173 processes, along with subtleties such as the inclusion of antecrystic minerals, produce
174 disequilibrium mineral assemblages that provide valuable insight into the latest stages of
175 magmatism (Couch et al., 2001; La Spina et al., 2016; Ubide et al., 2014; Zellmer et al.,
176 2016; Zellmer et al., 2014). Thus, for natural magmatic systems, brief durations on the order
177 of hours represent an end member in an ascent period context, and disequilibrium
178 characteristics may be useful if properly placed into a petrogenetic context. Given boninite
179 petrogenesis occurs at relatively shallow depths and generates hot and hydrous melts,
180 sometimes in extensional settings (Reagan et al., 2017), rapid ascent rates cannot be
181 precluded. Furthermore, since it is possible that chromites preserved in boninite matrices may
182 have been generated within the source regions of the melts, knowledge of how these minerals
183 react to changes in the physiochemical states of the melts (i.e. experimental observation) is
184 needed in order to assess and contextualize natural sample materials. These considerations
185 provide an incentive to perform experiments on brief timescales and to analyse
186 disequilibrium features.

187 3. ANALYTICAL METHODS

188 Analytical facilities at Victoria University of Wellington, Hokkaido University, Massey
189 University, and The University of Iowa were utilized to gather the data presented here.

190 Following removal of the sample holder from the IHPV, each capsule was weighed to assess
191 for mass loss during the experiment. The capsules were then mounted in epoxy and ground to
192 expose their interiors. Ni-Pd alloys recovered from each sensor capsule was separated from
193 powdered ZrO₂ and mounted in epoxy. These sample materials were then polished for
194 imaging and microprobe analysis, using SiC lapwheels and diamond grit paste.

195 3.1. *Electron microbeam techniques*

196 Samples produced at ISTO were imaged using an FEI Quanta 200 Environmental scanning
197 electron microscope (SEM) at the Manawatu Microscopy and Imaging Centre (Massey
198 University). This SEM was also used to perform semi-quantitative analyses of calcic silicate
199 minerals using an attached EDAX energy dispersive spectroscope (EDS). Samples produced
200 at GSJ were imaged at the Creative Research Institute of Hokkaido University using a JEOL
201 JSM-7000F Field Emission SEM. An attached XMAX 150 EDS was used here to analyse the
202 capsule Pt walls in contact with sample melts in order to detect iron loss after each
203 experiment (Supplemental Text 2, Table S3). Quantification of Fe in Pt was achieved by
204 calibrating signal intensity to pure Co.

205 Electron probe microanalysis (EPMA) occurred at multiple laboratories: at Victoria
206 University of Wellington and The University of Iowa, JEOL JXA-8230 Superprobes were
207 used. Additional chromite analyses were performed at Hokkaido University on a JEOL JXA-
208 8800R. Glass analyses were performed using Na-migration mitigation techniques. In addition
209 to using diffuse beam conditions (spot sizes of 5-10 µm), two Na acquisitions are totalled. If
210 analyses return low concentrations (determined using secondary standards), then sodium loss
211 may be corrected by either: removing the second acquisition (if Na is lost), removing either

212 point (if either indicates loss), or back-calculating time-resolved intensity to correct for Na
213 loss. No analyses reported here experienced significant sodium migration as indicated by
214 multiple analyses of both sample and standard materials.

215 Secondary standards provided by the Smithsonian Institution Department of Mineral Sciences
216 and/or the Max Planck Institute for Chemistry were included in all glass and mineral
217 analyses. Ni-Pd sensor compositions were quantified using metal standards by Astimex.
218 Repeat analyses of secondary standards provided a basis to assess the accuracy of data
219 gathered during EPMA (Tables S1-S2, and S4). The accuracies associated with glass analyses
220 have been determined to be within 1% for SiO₂, Al₂O₃, MgO, and CaO, 5% for TiO₂, FeO,
221 and K₂O, 10% for Na₂O, and 20% for MnO. For analyses of silicate minerals, SiO₂, MgO,
222 CaO, and Na₂O are accurate to within 1%, while FeO, Cr₂O₃, MnO, and Al₂O₃ are better than
223 2%. Chromite standardization was achieved using several mineral and oxide standards.
224 Replicate standard analyses demonstrated that all major elements given are accurate to within
225 5%, while MnO is accurate to within 40%. Secondary standard compositions are taken from
226 Jarosewich et al. (1980); Jochum et al. (2006); and Jochum et al. (2005).

227 To ensure analyses of pyroxene were of high quality, raw EPMA data were normalized prior
228 to formulae recalculation using the methods described by Putirka (2008). Analyses that
229 returned cation totals much greater than or less than 4 (on an O = 6 basis) were discarded. In
230 a similar manner, raw chromite analyses were recalculated to cation proportions per 4
231 oxygens. Recalculation of ferric iron proportions used the equation of Droop (1987). No
232 other multivalent cations (e.g. Mn, Cr) were considered.

233 3.2. *Determination of phase proportions*

234 In order to provide high-precision phase proportion data, a computationally inexpensive
235 machine learning tool enabled the analysis of backscattered electron (BSE) images and

236 produced segmented images that we interpreted in terms of phase proportions using Adobe
237 Photoshop. Segmented images are images that have been petrographically interpreted using a
238 machine learning algorithm and are color-coded based on which phase each pixel represents
239 (Supplemental Text 3). The machine learning tool used is called Trainable Weka
240 Segmentation, and was developed by Arganda-Carreras et al. (2017). The algorithm requires
241 limited user input (5-8 user-defined groups of pixels) to “train” the computer-generated
242 classifier, which segments as many mineral phases as the user defines. This tool produced the
243 segmented images used to infer the phase proportions given in Table 2. The tool is provided
244 as a plugin on the Fiji Is Just ImageJ (FIJI) platform (Schindelin et al., 2012). A minimum of
245 5 training sessions were conducted for each analysis, and the data derived from each
246 segmented image were averaged to produce the given proportions with the calculated
247 standard deviation providing the precision of each phase classification. Images representative
248 of the sample textures were used for segmentation. See Supplemental Text 3 for more
249 information and an example of a segmented image.

250 3.3. *Determination of oxygen fugacities from the solid sensors*

251 Fugacity calculations were performed following the methodology of Scaillet et al. (1995).
252 Sensor compositions, X_{Ni} ($Ni/[Ni+Pd]$ calculated using cation proportion), were determined
253 following EPMA. Further discussion of fugacity, including the calculation methodology, is
254 provided in the Supplemental Text 1.

255 4. RESULTS

256 Weighing the capsules after quench indicated that no mass was lost during any experiment.
257 Table 2 gives information on each sample including the mixture used, initial water
258 concentration, experimental conditions, resultant phase proportions inferred for each sample,
259 sensor compositions, and fO_2 data.

260 The capsule interiors of every sample except for Bon1200Ub were analysed via EDS in order
261 to assess the degree of iron loss from the melt to the Pt of the capsule wall. Line analyses
262 from the sample-wall contact into the capsule wall yielded no detectable iron *c.* 30 μm from
263 the interface. Integrating concentration profiles demonstrates that iron loss in unbuffered
264 experiments is limited to 10% or lower (of bulk sample Fe), while buffered experiments lost
265 20-35% Fe over experiment durations (Supplemental Text 2, Table S3). However, we will
266 demonstrate that none of our discussion topics have been significantly affected by iron loss.

267 4.1. Petrographic observations

268 Euhedral-subhedral orthopyroxene (opx) is abundant and is the only silicate phase present at
269 1200°C and 1150°C (Figure 1A). In BSE images, these crystals often have bright caps that
270 form at the apices of euhedral crystal forms (Figure 1B). At 1100°C, a petrographically
271 distinct trace silicate phase was observed along with abundant opx in Bon1100U (Figure 1C).
272 Semi-quantitative EDS analyses of this phase demonstrate that this silicate is rich in Ca, Mg,
273 and Fe. If it is a pyroxene, it is likely augite (*c.* $\text{Wo}_{31}\text{En}_{57}\text{Fs}_{12}$). Chromite is stable in all
274 boninitic samples, and BSE images of moderate-sized grains show that chromite mantles
275 have become brighter than cores (Figure 1D), indicating that diffusive equilibration was
276 interrupted by quenching in large grains. In general, all chromites appear as anhedral grains
277 with sharp-subrounded corners. These are not indications of chromite growth, suggesting that
278 all observed chromites are the original seeds added to each experiment. Likewise, there is no
279 evidence of dissolution, which indicates that chromite was a stable phase for the full duration
280 of each experiment. This implies that our experiments only produced pyroxene crystallization
281 in the presence of stable chromite.

282 A small number of micro-vesicles occur in all boninitic samples (e.g. Figure 1A). The
283 vesicles are spherical and show no indication of clustering. They appear randomly distributed
284 within the sample volume. No vapour films were observed along any of the capsule walls.

285 4.2. *Redox sensors and calculation of imposed fO_2*

286 Average X_{Ni} values were calculated for each sensor and used to infer sensor fO_2 for each
287 experiment. For water undersaturated sample melts, a_{H_2O} must be modelled in order to
288 accurately calculate fO_2 . To this end, the activity model of Burnham (1979) was used in
289 conjunction with major element data and inferred melt water concentrations (Supplemental
290 Text 1) to model a_{H_2O} . The uncertainties reported here for fO_2 are similar to those reported
291 elsewhere for the solid sensor technique (Jégo et al., 2010; Scaillet et al., 1995). The
292 solubility model of Zhang et al. (2007) was used to calculate maximum water concentrations
293 in residual melts under the experimental conditions, which correspond to *c.* 5.3-5.4 wt%.
294 According to these model constraints, boninitic melts did not reach saturation (Table 2), and
295 the ubiquitous presence of micro-vesicles (Figure 1A) is therefore not due to water saturation
296 (exsolution) but likely due to the inclusion of atmospheric gas in the sample capsules during
297 preparation.

298 Complexities associated with quench crystallization were observed in samples Bon1200Ua
299 Bon1200Ub, Bon1200Ba and Bon1200Bb and are discussed later. A principal effect of
300 quench crystallization is to raise a_{H_2O} in residual melts. Thus, for these high-T samples, the
301 reported fO_2 data are considered maxima.

302 4.3. *Compositional Data*

303 Representative compositional data are given in Table 3. Full sample datasets for each phase,
304 including secondary standard analyses, data compiled from the literature, and model data, are
305 given in Tables S1-S2 and S4. Literature data cited for comparison are provided in Table S5.

306 4.3.1. Glass compositions

307 Residual melts formed andesitic glasses, the compositions of which are given with other
308 experimental products in Table 3. These glasses are depleted in FeO, MnO, MgO, and Cr₂O₃
309 relative to both the initial boninite glass as well as the bulk composition of the system
310 (Table 1). SiO₂, CaO, Al₂O₃, Na₂O, K₂O, and TiO₂ are enriched in residual melt during every
311 experiment, which is consistent with extensive opx crystallization.

312 The two experiments conducted at high temperature (Bon1200U and Bon1200B) returned
313 four samples with glasses containing low MgO concentrations relative to those from
314 experiments conducted at 1150°C. This is counterintuitive, because the crystallization of opx
315 at higher temperature should produce a lower proportion of minerals relative to lower
316 temperatures, and overall depletion of MgO and FeO relative to the initial glass composition
317 should be smaller. Additionally, glass compositions inferred for sample Bon1200Ua indicate
318 a high degree of heterogeneity beyond the limit of analytical uncertainty, consistent with
319 inefficient quenching producing local melt heterogeneity. These data, along with relatively
320 high melt K₂O concentrations and the presence of abundant rim formation on opx grains
321 within these samples (Figure 1B) indicate that a significant degree of quench crystallization
322 has occurred in the high temperature experiments. These observations are absent from all
323 experiments conducted at 1150-1100°C, which suggests that quenching was efficient in these
324 latter experiments and that no quench crystallization occurred.

325 4.3.2. Pyroxene compositions

326 Opx formed under every temperature and redox condition imposed by the IHPV. In order to
327 confirm the identity of low-Ca pyroxenes as opx and not pigeonite, we calculated calcium
328 molar fractions for an opx-clinopyroxene (cpx) dividing line using equation 38 of Beattie et
329 al. (1991) with the experimental temperatures imposed within the IHPV as the single
330 independent variable. All pyroxene data presented here fall below these model values, which
331 confirms their identity as opx. Opx compositions are graphically illustrated in Figure 2.
332 Plotted alongside these data are data taken from other experiments conducted using boninitic
333 bulk compositions (Tatsumi, 1981; Umino and Kushiro, 1989) and natural opx compositions
334 sourced from boninitic rocks (Mariana trench, Bloomer and Hawkins, 1987; Troodos
335 ophiolite, Cameron, 1985; and Chichijima, Umino, 1986; Yajima and Fujimaki, 2001).

336 Opx Mg# (molar Mg/[Mg+Fe_{Total}]) positively correlates with temperature, and under buffered
337 redox conditions is lower than in unbuffered products (Figure 2). Differences in MgO and
338 FeO concentrations observed in samples processed at 1200°C but different fO_2 are on the
339 order of 1-2 wt% for each element. Thus, lower Mg# is associated both with lower
340 temperature as well as lower fO_2 . Minor oxide components in opx include CaO, Na₂O, Cr₂O₃,
341 MnO, TiO₂, and Al₂O₃. The concentrations of each of these oxides are < 5 wt%, with
342 variation of some concentrations correlating with changes in the intensive parameters of the
343 IHPV. Higher cation proportions of Ca, Al, and Mn are observed in samples synthesized
344 under lower temperatures (Figure 2). Cr₂O₃, Na₂O and TiO₂ concentrations are extremely low
345 in all pyroxenes, and potential variations in these oxides due to changes in temperature or
346 redox condition are imperceptible when considering the detection limits for these elements.

347 The effects of imposing variable redox conditions on the melt-opx partitioning of Ca, Al, and
348 Mn cannot be discerned for a given temperature interval because, with regard to these
349 elements, the mean core compositions for all opx synthesized at a given temperature are not
350 observed to significantly change between high and low fO_2 .

351 When natural and other experimental opx compositions are compared to the experimentally
352 synthesized opx presented here, the majority of natural and experimental opx compositions
353 are similar to opx synthesized at 1200°C and under buffered fO_2 conditions in terms of their
354 Mg#. Mn proportions broadly overlap with products of high temperature crystallization,
355 while Al and Ca cation proportions from the literature are, respectively, somewhat lower and
356 higher than our experimental products.

357 4.3.3. Chromite compositions

358 Initial seed chromite fragments were analysed by EPMA in order to determine if the
359 chromite pod could be considered homogeneous. Representative data are given in Table 1
360 with other starting material compositions. A single analysis revealed minimal enrichment of
361 FeO and TiO_2 (Table S2). Because the level of enrichment is low and rarely observed, we
362 consider the seed chromite to be homogeneous.

363 Experimental chromite compositions are chromium-rich, typically with $70 < Cr\# < 81$ ($Cr\# =$
364 molar $Cr/[Cr+Al]$, Table 3), and compositional data are illustrated in Figure 3. Priority was
365 given to small seed chromites (*c.* 10-15 μm in diameter) that were able to be analysed without
366 significant Si-contamination of the analysis volume from adjacent glass. This was because
367 the initial goal of adding seed chromite was to foster mineral growth from the boninitic
368 liquid. Since this likely did not occur, then the next best action was to analyse material that
369 most likely equilibrated with residual melts by the end of each experiment. Two samples
370 seeded with large chromite fragments (Bon1200Ua and Bon1200Ba) were observed to also
371 contain several small anhedral chromite fragments distributed among the opx crystals
372 (possibly chromite powder contamination from the sieving process). Several of these were
373 analysed in Bon1200Ua, but no analyses of chromite in Bon1200Ba were determined to be

374 free of glass contamination based on high observed concentrations of Si, Ca, and, in some
375 cases, Na. These data were rejected.

376 Compositions taken from the literature on boninite-hosted chromites sourced from the
377 Mariana trench wall (Bloomer and Hawkins, 1987), the Troodos ophiolite (Bailey et al.,
378 1991; Cameron, 1985; Flower and Levine, 1987; MacLeod, 1988; Thy and Xenophontos,
379 1991), Guam (Reagan and Meijer, 1984), and Chichijima (Umino, 1986) are provided for
380 comparison. Note that the chromites from Thy and Xenophontos (1991) are olivine-hosted
381 mineral inclusions.

382 In terms of trivalent cation proportions (i.e. Fe^{3+} , Al, and Cr), $f\text{O}_2$ buffered experiments
383 produced chromites with compositions that did not significantly change from the initial seed
384 composition (Figure 3A). Chromium is efficiently oxidized above NNO in iron-bearing melts
385 (Hanson and Jones, 1998). Thus, all Cr in chromite is Cr^{3+} . However, some of these
386 chromites have bright mantles that clearly indicate Fe enrichment (e.g. Figure 1D). Under
387 intrinsic $f\text{O}_2$ conditions corresponding to *c.* 3.2-4.0 log units above the NNO buffer and at
388 temperatures of 1200-1150°C (red and yellow diamonds on Fig. 3), significant amounts of
389 Fe^{3+} were added to chromite, resulting in an enrichment of total FeO with concentrations > 20
390 wt%. For these samples, their trend on Figure 3A illustrates significant Fe^{3+} -Al exchange
391 between chromite and melt, as the trend of core compositions runs sub-parallel to lines of
392 equal Cr proportion (which caused the observed increase in Cr# for these chromites). Because
393 this trend is linear and the samples do not cluster, it is likely that the Fe^{3+} -Al exchange
394 reaction failed to reach equilibrium. It is noteworthy that chromite grains in sample
395 Bon1100U appear to have lost very little Al during the experiments, as Al_2O_3 concentrations
396 are ≤ 1 wt% different from concentrations in the seed chromite, consistent with the observed
397 invariance of their inferred Fe^{3+} contents. TiO_2 was consistently low in all chromites,

398 reaching a maximum value of 0.14 wt% under the lowest temperature setting (Bon1100U).
399 NiO concentrations were nearly constant throughout the dataset at *c.* 0.11 wt%.

400 The literature data lie on a separate trend on Figure 3A that is sub-parallel to lines of constant
401 Fe^{3+} proportion. Of these data, chromite inclusions in olivine from the Kythreotis locality
402 (Troodos, Thy and Xenophontos, 1991) and matrix chromite from Guam appear to be the
403 most aluminous, while sample material from the Mariana Trench and Chichijima plot
404 together near the extreme Cr end of the ternary diagram along with other Troodos chromites.
405 In fact, chromite compositions from Troodos boninites and tholeiites span a wide range on
406 this diagram, plotting between the Kythreotis samples and the highly chromian composition
407 observed for the Kapilio locality (Cameron, 1985). The similarity between some of the
408 chromites observed in Troodos boninites/tholeiites and the seed chromites from the plutonic
409 chromitite is noted, as it was by Cameron (1985).

410 In Figure 3B, Mg# (chromite $\text{Mg\#} = \text{Mg}/[\text{Mg} + \text{Fe}^{2+}]$ using molar proportions) is plotted
411 against $\text{Fe}^{3+}/[\text{Fe}^{3+} + \text{Cr} + \text{Al}]$ (also calculated using molar proportions) in order to visualize the
412 effects of iron enrichment in a compositional space that is more representative of the spinel
413 (*sensu lato*, hereafter *s.l.*) solid solution. Again, it is evident that buffered experiments
414 (squares) have the same Fe^{3+} proportion as seed chromite. However, it is apparent that some
415 Mg- Fe^{2+} exchange has occurred at 1150°C, which represents the rim formation reaction
416 observed in BSE images (yellow square). Thus, in $f\text{O}_2$ buffered experiments conducted at
417 1150°C, Fe^{2+} has been added to chromite and Mg has been lost to the melt. For a given
418 temperature, Mg# appears to decrease with Fe^{3+} incorporation. This is observed for samples
419 recovered from experiments Bon1200U and Bon1150U, which plot to higher Fe^{3+} relative to
420 products of buffered experiments. Interestingly, natural chromite compositions observed in
421 the Troodos ophiolite span a slightly greater range of Mg# than the experimental products.

422 Included in these data are additional olivine-hosted chromite inclusion data from Sobolev et
423 al. (1993) and Golowin et al. (2017).

424 5. DISCUSSION

425 5.1. *Assessment of divalent cation distribution and equilibrium state between chromite-* 426 *opx-melt*

427 Because the experiments described here did not produce any discernible chromite growth,
428 instead of discussing chromite crystallization, the following sections discuss the state and
429 kinetics of chromite equilibration. The physiochemical states imposed upon the boninite
430 system are analogous to a shallow-mid crust setting, and thus these experiments are ideally
431 suited to study the effects of chemical disequilibrium on compositional change as a function
432 of temperature and fO_2 over brief timescales in this setting.

433 Based on textural evidence, it is apparent that large seed chromites in the samples presented
434 here failed to reach chemical equilibrium with their residual melts (Figure 1D). Since opx
435 crystallization is the process that altered the major element composition of melts during each
436 experiment, it is also the process that determines the extent to which chromite would have to
437 interact with residual melt in order to reach an equilibrium state under the conditions imposed
438 within the IHPV. Thus, it is important to qualify the relationship between opx and residual
439 melt so that chromite-melt relationships can be confidently explored.

440 In order to test for opx-melt equilibrium, the methodology of Putirka (2008) was used.
441 Specifically, for a given sample, melt cation fractions were calculated (X_d^{liq} , Table S1) for
442 each glass analysis. From these values, X_{Si}^{liq} was used to calculate model equilibrium Fe-Mg
443 exchange coefficients (K_D , Table 4, Figure 4A) using the following relationship given by
444 Putirka (2008):

$$K_D(\text{Fe} - \text{Mg})^{\text{opx} - \text{liq}} = 0.4805 - 0.3733X_{\text{Si}}^{\text{liq}} \quad \text{Equation 1}$$

446 An uncertainty (1σ) of ± 0.06 was attributed to these modelled K_D values, which is an order
447 of magnitude higher than the 1σ associated with the distribution of modelled K_D values given
448 in Table 4 and is illustrated as areas on Figure 4A. Observed K_D calculations employed molar
449 proportions for opx core analyses and average molar proportions for glass compositions.

450 Average K_D values (including 2σ error bars) for samples Bon1150U and Bon1150B plot
451 completely within their model areas, indicating that the opx sampled in these charges were in
452 equilibrium with their respective residual melts at the time of quenching. K_D values
453 calculated for three opx cores in sample Bon1100U produce an average K_D that is positioned
454 just outside of the model area. However, since the lower error bar stretches into the
455 uncertainty envelope as illustrated, it is reasonable to say that these crystals also equilibrated
456 with their residual melt. There are two negative effects of quench crystallization that
457 impacted K_D calculations and prevented us from determining whether opx in samples
458 processed at 1200°C were able to reach equilibrium or not. The first is the effect of raising
459 $X_{\text{Si}}^{\text{liq}}$, which occurred as quench crystals removed Mg, Fe, and Ca from residual melts. This
460 lowers model K_D values (Equation 1). The other effect is the removal of Mg and Fe from the
461 melt phase, which precluded realistic K_D values from being observed (Figure 4A). Since opx-
462 melt K_D s indicate an equilibrium condition for experiments conducted at $1150\text{-}1100^\circ\text{C}$, none
463 of the iron loss observed in these samples had an observable effect on the equilibrium
464 partitioning of Fe-Mg between opx and melt. This indicates that our equilibration
465 considerations are not significantly affected by this process.

466 In order to assess for chromite-opx equilibrium, the model of Liermann and Ganguly (2003)
467 was applied. This model was calibrated at higher pressures than imposed in our experiments.
468 However, because changes between partial molar volumes (of end-member compositions at

469 the standard state) associated with the Fe²⁺-Mg exchange reaction between chromite and opx
 470 appear to exhibit ideal mixing behaviour and because both Fe²⁺ and Mg endmembers exhibit
 471 similar and predictable pressure dependencies, Liermann and Ganguly (2003) assumed a
 472 pressure normalization scheme (their equation 5) to process their K_D values and formulate a
 473 thermometer for opx-chromite pairs that may be applied under a wide range of pressure
 474 conditions. We have rearranged this thermometer (their equation 8) to predict chromite-opx
 475 K_D (Fe²⁺-Mg, Table 4) at 2 kbar (0.2 GPa):

$$476 \quad K_D(\text{Fe}^{2+} - \text{Mg})^{\text{chrom} - \text{opx}} = \exp \left[\frac{AT(\text{K}) + B + 122P(\text{GPa}) - CX_{\text{Al}}^{\text{opx}} + DY_{\text{Cr}}^{\text{chrom}}}{T(\text{K})} \right] \quad \text{Equation 2}$$

477 This K_D equation utilizes opx Al molar proportion ($X_{\text{Al}}^{\text{opx}}$), chromite Cr/[Cr+Al+Fe³⁺]
 478 ($Y_{\text{Cr}}^{\text{chrom}}$), and constants derived for Al-Fe³⁺ system correction using the charge balance
 479 method: A = -0.351±0.102, B = 1217±120, C = 1863, and D = 2345±188 (Table 4 of
 480 Liermann and Ganguly, 2003). Uncertainties associated with the model K_Ds were calculated
 481 to be ±0.157 (i.e. better than ±7%, 2σ relative) based on propagating the uncertainties
 482 provided for coefficients A, B, and D. Assuming the compositional parameter for opx does
 483 not significantly change, and since Cr proportions for the synthetic chromites are not
 484 observed to change significantly between any of the samples (Figure 3A), this equation
 485 predicts the equilibrium state of chromite-opx with regard to Fe²⁺-Mg exchange for each
 486 experimental condition at the time of quenching (Figure 4B, observed K_D values were
 487 calculated using molar proportions with chromite X_{FeO} multiplied by molar Fe²⁺/ΣFe inferred
 488 from stoichiometry).

489 As illustrated on Figure 4B, the Fe²⁺-Mg subcomposition of chromite (given as Mg# in
 490 Figure 3B) in several samples has equilibrated with the opx-melt subsystem over the brief
 491 timescale of these experiments. The relatively large seed shown in Figure 1D has a rim that is
 492 *c.* 8-10 μm wide. Because our analyses prioritized small chromites that were *c.* 10-15 μm in

493 diameter, we consider it likely that EPMA sampled chromite that completely equilibrated
494 with respect to Fe²⁺-Mg through diffusion.

495 Thus, since a self-consistent determination of equilibrium has been established using
496 empirical relationships, then the Fe²⁺-Mg data provided here describe the equilibrium
497 condition of the melt + opx + chromite system under high temperature and fO_2 conditions
498 analogous to those in sub-arc crust. Interestingly, significant degrees of iron loss should raise
499 the Mg# of the sample bulk composition even when the ratio of Fe²⁺ to Fe³⁺ in melt is
500 maintained by hydration (Supplemental Text 2). This effect should be observable in product
501 opx compositions, as higher melt Mg# should result in higher opx Mg#. Since this is not
502 observed (Figure 2, Table 3), then the observed iron loss (in the case of Bon1150B, 20% bulk
503 Fe) does not significantly affect the equilibrium distribution of Fe²⁺-Mg under our
504 experimental conditions.

505 *5.2. Assessing chromite-melt equilibrium based on model equilibrium trivalent cation*
506 *proportions*

507 Since Fe²⁺-Mg has now been accounted for, it is prudent to also examine the equilibrium state
508 of the trivalent cations in chromite. To this end, multiple modelling methods were integrated
509 to predict equilibrium chromite compositions (with respect to trivalent cation proportions).
510 Our method modelled system compositional data using the alphaMELTS front end (Smith
511 and Asimow, 2005) and the MELTS thermodynamic model (Ghiorso and Sack, 1995) with
512 Rhyolite-MELTS system corrections enabled (Gualda et al., 2012). Nested modelling utilized
513 SPINMELT-2.0 (Nikolaev et al., 2018a, b), which calculated an alternative stable chromite
514 composition for each intermediate MELTS step. These models are likely to bookend actual
515 trivalent cation proportions in spinel (*s.l.*) compositional space (see Davis and Cottrell, 2018;
516 Nikolaev et al., 2018a, for information and discussion on how individual models behave

517 when predicting chromite compositions). A detailed description of the modelling
518 methodology is included in Supplemental Text 4. SPINMELT-2.0 cannot make sense of
519 MELTS-modelled liquid compositions at NNO+3 because the liquid composition at this
520 condition lies outside of the calibration range for the SPINMELT-2.0 algorithm. Thus,
521 SPINMELT-2.0 data are not available under highly oxidizing conditions.

522 Figure 5 illustrates the relationship between MELTS and SPINMELT-2.0 models and the
523 difference between modelled compositions and the synthetic chromites produced in our
524 experiments. Alternative models were created to observe the effect of 30% iron loss on the
525 system (empty symbols, Figure 5). It appears that under highly oxidizing conditions and
526 1150-1200°C, experimental chromite $\text{Fe}^{3+}/[\text{Fe}^{3+}+\text{Cr}+\text{Al}]$ values approach values that are
527 attained at NNO+2 in the MELTS models. Still, given the distance on the ternary diagram
528 between modelled chromite compositions and our experimental data, none of the
529 experimental chromites are in equilibrium based on observed trivalent cation proportions.
530 This includes model data that were generated under conditions where iron loss was accounted
531 for. The principal effect of iron loss is to reduce the proportion of iron in equilibrium
532 chromite. The trend to high Fe^{3+} concentrations observed for the oxidized samples illustrated
533 in Figures 3A and 5 are likely to represent a segment of a diffusion trend in ternary space.
534 The concept of diffusion in this compositional space is explored below. Since the volume of
535 chromite in the charges is invariant (i.e. no resorption or crystallization has been observed),
536 then the process by which chromite equilibrates can exclusively be attributed to diffusion.

537 Differences between MELTS and SPINMELT-2.0 output data are surprisingly large but may
538 be attributed to both our modelling strategy (Supplemental Text 4) as well as inherent
539 limitations of the model platforms. Models in the MELTS family tend to overpredict spinel
540 (*s.l.*) Fe^{3+} proportion and underpredict Cr proportion (Davis and Cottrell, 2018; Nikolaev et

541 al., 2018a), and the creators of SPINMELT-2.0 claim that their model reproduces several
542 petrologically important chemical aspects of chromite chemistry to better than 20% (Cr/Al
543 and Mg/Fe²⁺, Nikolaev et al., 2018a). What MELTS does describe accurately is Fe-Al
544 exchange within the system during melt evolution and thus likely provides a best fit topology
545 in compositional space (Davis and Cottrell, 2018). Because of these observations, we
546 reiterate that our modelling method likely bookends equilibrium chromite compositions;
547 keeping in mind that multiple experiments were performed beyond the calibration range of
548 SPINMELT-2.0.

549 In the case where Fe²⁺ in chromite is in equilibrium with the co-existing melt/silicate mineral
550 assemblage, the interdiffusion of trivalent cations should occur in chromite with Fe²⁺/Fe³⁺
551 higher than that in coexisting melt, as melt Fe²⁺/Fe³⁺ should always be higher than spinel
552 Fe²⁺/Fe³⁺ (Maurel and Maurel, 1982). Using equation 7 of Kress and Carmichael (1991),
553 model melt Fe²⁺/Fe³⁺ values were generated (Table S1) using glass compositions and the
554 intensive parameters imposed by the IHPV to show that most if not all experimental
555 chromites must incorporate more Fe³⁺ before reaching an equilibrium Fe²⁺/Fe³⁺ threshold
556 (Figure 6). That is, in order to reach an equilibrium condition, the observed Fe²⁺/Fe³⁺ in
557 chromite must incorporate more Fe³⁺ so that their ratio values fall below the grey lines on
558 Figure 6. The exception is sample Bon1200Bb, the chromite Fe²⁺/Fe³⁺ values of which are
559 distributed (mostly) beneath the modelled melt Fe²⁺/Fe³⁺ value.

560 The diffusion of major cations within spinel (*s.l.*, e.g. Figure 19 of Van Orman and Crispin,
561 2010) are ranked by order of decreasing diffusivity (log D, m²/s) at 1100°C (10⁴/K = *c.* 7.3):
562 Mg-Al (extrapolated, *c.* -13.5), Fe (self-diffusion, *c.* -16), Mg (self-diffusion, *c.* -16.5), and
563 Cr-Al (below x-axis, see below). Thus, D_{Cr-Al} is likely the limiting factor in chromite-melt
564 diffusive equilibration, though uncertainties associated with D_{Cr-Al} are reportedly large at high

565 Cr# (Suzuki et al., 2008) and fO_2 affects D_{Fe} (Vogt et al., 2015). As stated by Vogt et al.
566 (2015) this behaviour is not well constrained under high-T and high-P conditions. Our results
567 corroborate this inference. Since spinel (*s.l.*) is an isometric mineral, the given diffusivities do
568 not vary with crystallographic orientation, which is convenient for the purpose of textural
569 analysis (Supplemental Text 5).

570 As demonstrated in Figure 3A, when buffered at NNO+0.4, +1 and +2.5, chromite
571 compositions did not significantly change from the original seed composition with respect to
572 trivalent cation proportion. Only change in Mg# is observed for these chromites (Figure 3B).
573 Significant Fe^{3+} incorporation was only observed in unbuffered samples at $T > 1100^\circ C$ and
574 occurred at the expense of Al, since trivalent cation proportions for these samples are
575 distributed along lines of equal Cr proportion (Figure 3A). Thus, Al counter-diffusion
576 facilitated Fe^{3+} incorporation in chromite under highly oxidizing conditions at 1150-1200°C;
577 although it is unlikely these minerals completely equilibrated during the experiments
578 (Figure 5).

579 The Fe-Mg and Fe-Al exchange reactions have also been observed in natural samples that are
580 allowed to equilibrate over decadal timescales (Scowen et al., 1991). Importantly, the
581 observations of Scowen et al. (1991) confirm the rank of the diffusivities outlined above and
582 establish that even though Cr is the most sluggish element to diffuse, eventually Cr diffusion
583 does occur in natural settings to equilibrate chromite following Fe-Al interdiffusion.

584 Based on our observations, we hypothesize that Fe^{3+} -Al interdiffusion operates principally as
585 a function of fO_2 to equilibrate chromite Fe^{2+}/Fe^{3+} (after equilibration of chromite Mg#) on a
586 shorter timescale than is required to equilibrate Cr in the system. This scenario of diffusive
587 re-equilibration may be conceptualized within a multi-step chemical reaction (Figure 7). The
588 first step concerns Fe^{2+} -Mg exchange between chromite and melt. This is the only reaction

589 observed in samples processed under buffered fO_2 (and in sample Bon1 100U), and since the
590 observed changes in chromite composition are more complex under higher fO_2 conditions, we
591 combine this exchange with the observed increase in Fe^{3+} in trivalent cation proportion as
592 reaction 1 (Figure 7). Thus, a relatively high $Fe^{2+}/Mg + Fe^{3+}/Al$ composition is generated as a
593 magnetite component ($FeFe_2O_4$) is added to the starting chromite composition. This exchange
594 is facilitated by the counter-diffusion and exchange of Mg and Al, and the spinel (*sensu*
595 *stricto*, hereafter *s.s.*) component thus diminishes (see Table S2 for modelled end-member
596 component compositions). With reaction 1, the chromite composition approaches a tie line
597 between $Fe(Al,Cr)_2O_4$ and $Mg(Fe,Cr)_2O_4$ in the compositional space of the spinel (*s.l.*) prism
598 (dashed grey line in Figure 7A). Importantly, the chromite compositional trend will not
599 approach the Cr-magnetite solid solution in the prism space but a spinel (*s.l.*) composition
600 intermediate between Cr-magnetite and the $Mg(Fe,Cr)_2O_4$ solid solution, as spinel (*s.l.*) Mg
601 concentration is only being diluted by reaction 1 (i.e. Mg is rearranged within the chromite
602 matrix with some flux across the crystal-melt boundary). In order to equilibrate Cr
603 proportion, which is expected to decrease under all imposed experimental conditions
604 (Figure 5), compositions should evolve along lines of equal Fe^{3+}/Al (dashed grey line in
605 Figure 7B; reaction 2) in the isothermal state as Cr is lost to the melt phase. An added
606 component with higher Fe^{2+}/Mg is required because Mg# in chromite was not observed to
607 increase in any experiment (Figure 3B) and because this is necessary for chromite to
608 equilibrate with the silicate mineral assemblage (Figure 4B).

609 The difference in diffusivities between mineral species provides an interesting constraint on
610 the origin of the polymineralic microlite assemblages described here. In particular, Fe-Mg
611 interdiffusion in opx occurs more slowly ($\log D = -19.5$ at QFM and high T, Klügel, 2001)
612 than interdiffusion of any of the major cations in chromite. If, in natural samples, it is found
613 that microlitic silicates like opx are in equilibrium with residual melts and matrix chromites

614 are not, then the likely explanation for this observation is that the microlitic silicate formed
615 from the melt it is in (i.e. an equilibrium crystallization process). Crystallization of ferrous
616 phases is one of several oxidizing mechanisms in arc magmatic systems (see Cottrell et al.,
617 2020). This process provides an impetus for diffusive re-equilibration of chromite to begin,
618 and the grounds for oxyspeedometric analysis of the chromite-melt subsystem in a diffusion
619 chronometric context. Chromite crystals sampled from Chichijima (Umino, 1986), the
620 Troodos ophiolite (Bailey et al., 1991), and Guam (Reagan and Meijer, 1984) exhibit
621 chemical zonation consistent with pre-eruptive oxidation, as chromite rim-mantle zone
622 analyses return more ferric compositions than analyses of their cores. Such features are
623 unique to the pre-eruptive regime but may be confused with compositional trends that are
624 attributable to chemical weathering. Thus, it is important to discern here oxidation of
625 chromite that occurs in this scenario and oxidation that occurs post-eruption (i.e. chemical
626 weathering or metamorphism of chromite). In the literature on the zoned chromites described
627 above, there is no mention of textures consistent with porous-chromite oxidation (Gervilla et
628 al., 2019; Hodel et al., 2020). The volcanic rocks sampled by the studies cited above were
629 observed to be fresh with little to no evidence of alteration, which is not consistent with a
630 weathering environment capable of significantly modifying chromite compositions in either
631 hydrothermal (Hodel et al., 2020) or metamorphic (Gervilla et al., 2019) regimes. Instead,
632 since the chromite FeO and Al₂O₃ concentrations are observed to increase from core to rim
633 (which is a geochemical signature of magmatic oxidation in our model, i.e. reaction 2 of
634 Figure 7), we maintain that these zonation patterns are of magmatic rather than secondary
635 origin. With this in mind, the next sections assess natural chromite and glass compositions
636 recovered from the extrusive suite of the Troodos ophiolite in a similar manner as our
637 experimental products, and data available from the literature are used to constrain ascent rates
638 for these lavas.

639 5.3. *Experimental observations vs. natural processing in the crustal column*

640 Mafic Troodos glass compositions were taken from the literature for the following localities:
641 the Kalavassos Mine (eastern end of the Limassol Forest Complex), Margi (northern part of
642 the extrusive sequence), and Kapilio (western end of the Limassol Forest Complex). All data
643 were taken from Woelki et al. (2020) with an additional two glass analyses from Golowin et
644 al. (2017) for the Kalavassos Mine locality. The studies cited used laser ablation inductively
645 coupled plasma mass spectrometry to quantify minor-trace concentrations of Cr for these
646 samples. Data on mineral compositions for these locations are sparse. However, multiple
647 compositions were found and taken from Cameron (1985), Bailey et al. (1991), Flower and
648 Levine (1987), and MacLeod (1988). Here, we assess these data to determine if the
649 aforementioned minerals and melts were in equilibrium at the time of eruption. Chromite data
650 were found neither for the Akaki River Canyon section nor for the Arakapas Fault Belt
651 though Ohnenstetter et al. (1990) performed several analyses, no data are provided in the
652 source. Thus, even though these locations have been widely studied, we are currently unable
653 to assess for chromite-melt equilibrium for these parts of the extrusive sequence.

654 SPINMELT-2.0 was used to model equilibrium chromite compositions in a similar way as in
655 the experimental scenario discussed above. Physiochemical variables were set to approximate
656 eruption conditions with pressure set to 0.5 kbar, which corresponds to a water depth of 5000
657 meters (inferred eruption condition, Woelki et al., 2020), and the fO_2 of the system was set to
658 QFM+0.25 (*c.* NNO-0.5), QFM+0.75 (*c.* NNO), and QFM+1.25 (*c.* NNO+0.5). This range
659 compares well with the natural range of fO_2 for the Troodos magmas; crystallization of
660 olivine + chromite occurred at fugacities slightly above QFM+0.25 (Golowin et al., 2017);
661 and glasses recovered from a Troodos “upper pillow lava” (Rautenschlein et al., 1985) have
662 Fe^{2+}/Fe^{3+} (recalculated to molar ratios) that return fO_2 values \geq QFM+1.35 (NNO+0.6) using

663 a pressure of 0.5 kbar, a temperature of 1130°C (upper limit of eruption temperature given by
664 Golowin et al., 2017), a rearranged equation 7 from Kress and Carmichael (1991), and the
665 fugacity conversions of Frost (1991), providing a reasonable estimate for the upper limit for
666 our fugacity setting.

667 SPINMELT-2.0 output was treated in a similar way as the experimental data (Supplemental
668 Text 4). When fO_2 is provided, melt Fe^{2+}/Fe^{3+} is calculated internally and used to model
669 chromite composition. Since temperature is not provided to the program, it must be predicted
670 by the algorithm to provide a chromite composition estimate for each input melt composition.
671 For these lavas, liquid temperatures have been inferred to vary between *c.* 1030-1130°C
672 (Golowin et al., 2017). These temperatures are consistent with temperatures inferred from
673 viscosity models (Schouten and Kelemen, 2002) generated for lavas on the North side of the
674 extrusive sequence and with independent thermometry (inferred to provide a quantification of
675 closure temperature) performed by Dare et al. (2009) for the Kalavassos Mine locality.

676 SPINMELT-2.0 output was observed to lie within 25°C of this temperature range for a
677 majority of the glass samples (Table S6) for each fO_2 condition. Thus, we inferred that our
678 models faithfully replicated equilibrium conditions for chromite-melt at the time of eruption.

679 Figure 8 illustrates the relationships between modelled and observed chromite compositions
680 of the Troodos (cf. Figure 5). Sample glass recovered from the Kalavassos Mine produced
681 one major cluster for each fO_2 condition and one Al-rich glass sample displaced modelled
682 chromite compositions to higher Al and lower Cr. All glass samples were determined to be
683 “tholeiitic” by Woelki et al. (2020). All of the matrix chromite compositions observed for this
684 locality are similar to olivine-hosted chromite inclusions observed in these same lavas
685 (Golowin et al., 2017). A single natural chromite composition is displaced to higher Al
686 compared with the others. However, according to our models, all of these chromite

687 compositions are too Cr-rich and require $\text{Fe}^{3+}+\text{Al}$ incorporation to be in equilibrium with
688 residual melts.

689 Woelki et al. (2020) determined that the glass samples recovered from the Kapilio locality
690 range from boninitic to tholeiitic in composition. The chromite data from this locality include
691 the most chromian spinel (*s.l.*) analysis from the Troodos sample suite (Cameron, 1985) and
692 three relatively simple (number of elements reported = 4) analyses of chromite given by
693 Flower and Levine (1987). These compositions are also far from the modelled chromite
694 compositions. As with the samples from the Kalavassos Mine, $\text{Fe}^{3+}+\text{Al}$ incorporation is
695 required for re-equilibration. If a tie line is drawn through the natural samples from the Cr
696 apex, it would intersect the model array at the point where the data generated at QFM+0.75
697 touches the data generated at QFM+1.25.

698 Finally, chromites taken from the Margi locality exhibit a compositional trend that is similar
699 to that observed in the data from the Kapilio suite. Glasses taken from this locality produced
700 a high-Al and low-Al trend, which reflects a modest separation of the glass data into more
701 and less differentiated populations, respectively. Chromite core analyses given by Bailey et
702 al. (1991) lie in roughly the same area as those of the Kalavassos Mine. However, rim
703 analyses reported in this study are displaced to higher Fe^{3+} concentrations with a single
704 analysis reaching the Fe^{3+} proportion inferred for chromite in equilibrium with melt at
705 QFM+0.75. However, for this mineral rim, Cr-Al interdiffusion must also occur to reach the
706 Al concentration inferred to represent an equilibrium composition. Thus, we conclude that the
707 chromites observed in the Troodos extrusive suite were not in equilibrium with their residual
708 melt compositions at the time of eruption, but in multiple localities these minerals were likely
709 in a state of active equilibration (via diffusion) at the time they were erupted.

710 Regarding Fe^{2+} , slowly cooled chromites lose Mg to coexisting ferromagnesian silicates
711 (Ozawa, 1984), while rapidly quenched mineral pairs preserve high-temperature
712 compositions (e.g. Scowen et al., 1991). Since the glasses sampled from the Troodos rapidly
713 quenched upon eruption (e.g. Robinson et al., 1983), chromite Mg# may have been
714 preserved. By focusing on a single locality where glass, opx, and chromite data exist, we may
715 treat natural samples in the same way as the experimental products above and test for system
716 Fe^{2+} -Mg equilibrium. To this end, we refocus on the Kapilio locality. Glass data from this site
717 (Woelki et al., 2020) were processed to predict $K_D(\text{Fe-Mg})^{\text{opx-liq}}$ values using equation 1.
718 Mineral data from this locality are from Flower and Levine (1987). In total, two opx and
719 three chromite compositions were used (their sample AM-4, Table 5). Unfortunately, there is
720 no way of determining if these materials come from the same outcrops as the glass, which is
721 why all glass data were used in modelling. Based on model physiochemical constraints
722 outlined above, the opx sampled by Flower and Levine (1987) is in equilibrium with residual
723 melts (within 1σ of the mean model $K_D(\text{Fe-Mg})^{\text{opx-liq}}$ value). Using a median $Y_{\text{Cr}}^{\text{chrom}}$ for the
724 matrix chromites (0.70), model $K_D(\text{Fe-Mg})^{\text{chrom-opx}}$ values (calculated using equation 2) are
725 observed to vary between *c.* 4.68-4.96 at 1130°C and 0.5 kbar and 5.41-5.86 at 1030°C and
726 0.5 kbar (Table 5). Varying $Y_{\text{Cr}}^{\text{chrom}}$ by 0.1 (the actual variation observed among the sample
727 chromites) causes these model K_D values to vary by ± 0.07 (*c.* $\pm 3\%$), which is roughly one
728 half of the magnitude of the uncertainty associated with the model parameters. Observed
729 $K_D(\text{Fe-Mg})^{\text{chrom-opx}}$ values are found to vary between 4.8 and 7.3 depending on which
730 chromite-opx pair is used. Two of the three chromite grains are seen to be in equilibrium with
731 at least one of the opx grains based on these K_D models. One other chromite grain in this
732 sample returned high observed K_D values for both opx grains, reflecting low MgO
733 concentrations. This chromite also has a low total EPMA composition (94.79) compared to
734 the other analyses (*c.* 98). Regardless, it is remarkable, given the dearth of mineral data

735 available for the Troodos extrusive sequence, that any equilibrium condition could be
736 established at all. These findings further the point that more mineral data should be gathered
737 from the Troodos ophiolite and other natural chromite-bearing rocks to assess for mineral-
738 mineral/mineral-melt equilibrium.

739 The effects of natural quench crystallization and syn-eruptive microlite growth on modelling
740 equilibrium chromite composition also needs to be considered. Depending on the Fe-Mg ratio
741 of the minerals that crystallize, Fe^{2+} may be enriched or depleted in the residual melt. Using
742 equilibrium exchange coefficients (e.g. Putirka, 2008), the crystallization of ferromagnesian
743 silicates like olivine and opx are expected to enrich melts in FeO relative to MgO, and the
744 differentiation of melt by these minerals should modestly enrich Fe^{3+} over Fe^{2+} (Birner et al.,
745 2018; Kelley and Cottrell, 2012; O'Neill et al., 2018; Shorttle et al., 2015). Melt Al_2O_3 is
746 expected to increase with the equilibrium crystallization of ferromagnesian silicates. Based
747 on observations of the experimental products made at 1200°C, melt Al_2O_3 concentrations
748 were not significantly affected by quench crystallization (Table 3). Although this effect will
749 depend on the volume of crystallization produced during quenching, which was not
750 constrained, we do not expect minor degrees of quench crystallization to significantly affect
751 melt Al_2O_3 unless an aluminous phase crystallizes. In some relatively differentiated Troodos
752 lavas, plagioclase feldspar is observed (Flower and Levine, 1987; Schmincke et al., 1983).
753 Feldspar crystallization is expected to reduce melt Al_2O_3 and thus modelled chromite Al_2O_3
754 concentrations, which would cause observed chromite compositions to appear closer to
755 equilibrium. Instead, we propose that (i) the higher chromite Al concentrations predicted by
756 our modelling (Figure 8) reflect Al_2O_3 enrichment in the magmas (and thus the absence of
757 plagioclase in glasses sampled by Woelki et al., 2020) that comprise the Troodos extrusive
758 sequence, which is consistent with the predominate silicate mineral assemblages observed
759 therein; namely olivine, olivine+cpx, or olivine+opx+cpx (Flower and Levine, 1987; Malpas

760 and Langdon, 1984; Schmincke et al., 1983), and that (ii) quench crystallization does not
761 significantly affect these data. Since the most primitive glasses sampled by Woelki et al.
762 (2018) were observed to classify as boninite liquids, we infer that the most Cr-rich
763 equilibrium chromite compositions in our models (Figure 8), which correspond to these
764 relatively primitive melt compositions, represent chromite compositions that genuinely reflect
765 the equilibrium composition of chromite in melts unaffected by quench/syn-eruptive
766 crystallization.

767 5.4. *Estimation of maximum/minimum ascent time through diffusion modelling*

768 Since stable chromite was driven into chemical disequilibrium during magmatic
769 differentiation, remained in a state of disequilibrium with respect to trivalent cation
770 proportions at the time of eruption, and equilibrated with co-existing silicate minerals with
771 respect to Fe-Mg exchange (divalent cation proportion), magma ascent time may be
772 estimated on the basis of disequilibrium/equilibrium between chromite and the equilibrium
773 condition defined by the physiochemical state of the residual melts. Here, the maximum
774 ascent time was modelled based on the lowest interdiffusivity for the chromite compositional
775 system (D_{Cr-Al}), and minimum ascent time was modelled based on the highest interdiffusivity
776 (D_{Fe-Mg}).

777 Based on chromite-melt behaviour modelled above and observed in the mafic lavas of the
778 extrusive suite of the Troodos ophiolite, we estimated the maximum and minimum ascent
779 times by calculating the time (t) it would take to equilibrate a hypothetical groundmass
780 chromite microphenocryst [30-60 μm diameter with a composition similar to those of
781 primitive chromite microphenocryst cores and mineral inclusions from the Kalavassos Mine
782 locality (Figure 8, Golowin et al., 2017; Sobolev et al., 1993)] with residual melt under the
783 inferred eruptive conditions using the following relationship from Crank (1975):

784 $\tau = Dt/a^2$ Equation 3

785 where a is the crystal radius, t is time, τ is non-dimensional time, and D is the interdiffusion
786 coefficient.

787 $D_{\text{Cr-Al}}$, the interdiffusivity coefficient of Cr-Al in chromite, is positively correlated with both
788 temperature and Cr# (Suzuki et al., 2008). For this reason, we calculated $D_{\text{Cr-Al}}$ for chromite
789 with Cr# = 80 at 1030°C and 1130°C by extrapolating the relationships illustrated in Figures 5
790 and 10 of Suzuki et al. (2008) to low temperatures. In detail, we reproduced the Arrhenius
791 plot of Suzuki et al. (2008) for chromite with Cr# = 80 and fit linear equations to their
792 diffusivity data to predict $\log D_{\text{Cr-Al}}$ as a function of temperature (Supplemental Text 5). The
793 following equation was recovered:

794 $\log D_{\text{Cr-Al}} = -2.4199 \left(\frac{10^4}{T(\text{K})} \right) + 2.3902$ Equation 4

795 Using this equation, we estimate $\log D_{\text{Cr-Al}}$ (cm²/s) to be -16.2 at 1030°C and -14.9 at 1130°C
796 (Table 6).

797 We elected to use self-diffusion coefficients from Liermann and Ganguly (2002) to estimate
798 $\log D_{\text{Fe-Mg}}$ at the same conditions as $\log D_{\text{Cr-Al}}$. We also reproduced their Arrhenius plots for
799 both Fe and Mg self-diffusion (Supplemental Text 5) and then used their equation 4 to
800 calculate an interdiffusivity coefficient, $\log D_{\text{Fe-Mg}}$. For this calculation, we used the following
801 linear equations recovered from their Arrhenius plots:

802 $\log D_{\text{Fe}} = -1.0322 \left(\frac{10^4}{T(\text{K})} \right) - 4.7506$ Equation 5

803 $\log D_{\text{Mg}} = -1.0545 \left(\frac{10^4}{T(\text{K})} \right) - 4.7125$ Equation 6

804 Using these equations and equation 4 of Liermann and Ganguly (2002), $\log D_{\text{Fe-Mg}}$ was
805 calculated to be -12.7 at 1030°C and -12.2 at 1130°C (Table 6).

806 With these D values, we calculated maximum ascent time using the simple equation for
807 diffusion in a sphere (equation 3) by assuming $\tau = 0.04$ (i.e. insignificant change in core
808 composition) and minimum ascent time by assuming $\tau = 0.4$ (i.e. complete re-equilibration,
809 Table 6). At 1030°C, in order to preserve a matrix chromite core whose Cr# = 80, a maximum
810 of *c.* 170 years can pass before the core of the chromite begins to equilibrate, which means
811 that the mafic lavas of the Troodos ophiolite, once extracted from their mantle source,
812 crystallized their silicate cargo and erupted in less than *c.* 170 years. If T is raised to 1130°C,
813 the maximum amount of time is reduced to 8 years. Since the interdiffusivity coefficient is
814 positively correlated with Cr#, if chromite has a lower Cr# than 80, then maximum ascent
815 time increases. In fact, when Cr# approaches 0, $D_{\text{Cr-Al}}$ approaches values two orders of
816 magnitude lower than when Cr# = 80 (Suzuki et al., 2008). Maximum ascent times would
817 increase accordingly. However, because the chromites of the Troodos presented here are
818 highly chromian, we expect our maximum ascent times to be within reason. We calculated
819 minimum ascent time (for the same hypothetical chromite grain) at 1030°C to be *c.* 220 days.
820 At 1130°C this value is lowered to 60 days. These back-of-the-envelope calculations
821 demonstrate that it will be possible to constrain the ascent rate of boninitic magmas through
822 study of diffusion profiles in matrix chromite crystals that they carry, and this should be done
823 systematically in future research.

824 Overall, the melt temperature data cited as independent observations for the Troodos
825 extrusive suite are corroborative, but it is important to discuss these data because temperature
826 exerts strong control over diffusion. The three methods of temperature estimation are based
827 on geochemical modelling (Dare et al., 2009; Golowin et al., 2017; Schouten and Kelemen,

828 2002). Golowin et al. (2017) used olivine-melt compositional data and the equilibrium
829 relationships given by Ford et al. (1983) and Almeev et al. (2007) to quantify minimum
830 crystallization temperatures, which they interpreted as eruption temperatures. Schouten and
831 Kelemen (2002) used the geothermometer of Sisson and Grove (1993) to estimate
832 temperature for their viscosity models. Finally, Dare et al. (2009) calculated temperature
833 using the olivine-spinel thermometer of Ballhaus et al. (1991) and inferred this temperature as
834 a closure temperature for chromite. Taken together, since the present discussion is focused on
835 the kinetics of chromite-melt re-equilibration at pre-eruptive conditions, the estimates of
836 Golowin et al. (2017) represent our preferred liquid temperatures because they are most likely
837 to constrain melt temperatures prior to significant syn-eruptive crystallization of microlitic
838 pyroxene. Granted, when significant pyroxene crystallization occurs, melt water
839 concentrations assumed by Golowin et al. (2017) for Troodos glasses (*c.* 3 wt%) represent
840 maxima and their temperatures minima following the liquidus depression relationships given
841 by Almeev et al. (2007). Woelki et al. (2020) quantified water concentrations in boninite
842 glasses to be 1.7-2.7 wt%, which is slightly below the value provided by Golowin et al.
843 (2017). This means our models may use temperatures that are slightly underestimated. The
844 consequence of this is that our model ascent rates may be minima under high-temperature
845 conditions and that ascent times for the Troodos extrusive sequence may be higher than
846 modelled here. The likelihood of lower liquid temperatures are low due to the high closure
847 temperature of 1100°C inferred by Dare et al. (2009).

848 Additional complexity is added when considering the effect of changing Cr# during
849 oxidation. Since $\log D_{\text{Cr-Al}}$ becomes lower as chromite loses Cr (Suzuki et al., 2008), since we
850 elected to regress data provided for the highest Cr# chromites in the study of Suzuki et al.
851 (2008) in order to estimate maximum ascent rate, and since natural chromites have slightly

852 less Cr (Table S5), our maximum ascent times may be underestimated. This is an additional
853 knowledge gap that should be addressed with future experimental work.

854 Because primitive compositional characteristics of the oxide mineral cargo are retained in
855 several chromite crystals in the matrices of lavas of the Troodos ophiolite extrusive sequence
856 and because, in some cases, mineral textures relating to diffusive equilibration seem to be
857 preserved, we propose that chromites in such boninitic-tholeiitic lavas are products of either
858 (i) crystallization from primary magmas or the incongruent melting reaction that is known to
859 produce olivine + chromite in the shallow sub-arc mantle, or (ii) crystallization in complex
860 fluid-melt or melt-melt mixtures in the same part of the magmatic system. In either case,
861 chromite is likely precipitated prior to extensive pyroxene crystallization, as melt
862 fractionation by pyroxene tends to compromise chromite stability in some igneous systems
863 (e.g. layered mafic intrusions or ocean island basalts, Irvine, 1967; Roeder, 1994). Such
864 behaviour appears to be absent in boninites and tholeiites associated with ophiolitic terranes
865 such as the Troodos or the forearc regions of intra-oceanic arc systems (e.g. Whattam et al.,
866 2020). In these rocks, matrix chromite appears with stable pyroxene minerals as euhedral-
867 subhedral mineral grains with no signs of resorption or breakdown. Thus, chromite is most
868 likely a primitive component of the boninite-tholeiite petrogenetic system that perseveres
869 through differentiation in arc systems and likely records compositional traits that reflect the
870 full range of physiochemical states these magmas undergo prior to eruption (Figure 9).

871 In our petrogenetic model, synthesized in Figure 9, chromite forms in equilibrium with
872 primitive boninitic melt prior to the growth of many silicate minerals (Figure 9B) and has a
873 primitive composition characterized by high Mg# and Y_{Cr} (Stage 1). Once silicate minerals
874 nucleate (Figure 9C), chromite Mg# will immediately begin to re-equilibrate, as this
875 parameter is highly sensitive to the presence of ferromagnesian silicates (Stage 2). As these

876 silicates grow, melt oxidation occurs, and Fe^{3+} -Al exchange begins (Stage 3, Figure 9D).
877 Finally, Cr exchange begins to occur with Fe^{3+} and Al (such that chromite Fe^{3+}/Al remains
878 constant, Figure 7B) and the volume of chromite at the edge of the grain reaches an
879 equilibrium state with melt prior to eruption (Stage 4). If this chromite grain is entrained in an
880 ascending melt that is quenched upon eruption, then the differential diffusivities of the major
881 trivalent cations in chromite can be interpreted in a chronometric context (Figure 9E). Careful
882 analysis of chromite should include a quantification of Fe-speciation (see EPMA
883 methodology of Davis and Cottrell, 2018) so that precise thermometry and fugacity
884 information can be inferred from natural samples.

885 6. CONCLUSIONS

886 1) The experiments presented here enabled us to infer the kinetic behaviour of chromite
887 in boninitic melt. Pyroxene is a ubiquitous component of the experimentally
888 synthesized boninites, and residual melts are andesitic in composition. Matrix glasses
889 preserved in natural boninites (Coulthard Jr et al., 2021; Woelki et al., 2020)
890 demonstrate that olivine \pm pyroxene crystallization commonly generates residual
891 melts that are basaltic andesitic to andesitic in composition, similar to the products of
892 these crystallization experiments.

893 2) The fact that these same natural glasses are enriched in Fe^{3+} upon eruption (Brounce
894 et al., 2019; Rautenschlein et al., 1985) suggests that primitive boninitic melts (i)
895 crystallize chromite under less oxidizing conditions than those characteristic of the
896 pre-eruptive crustal column and within what are likely complex melt-fluid/melt-melt
897 mixtures present in the sub-arc or back-arc mantle, (ii) crystallize olivine/pyroxene
898 phenocrysts under magmatic conditions without significant chromite crystallization in
899 the crust, and (iii) entrain most of their chromite crystal cargo prior to microlitic

900 growth during ascent and eruption, to produce natural boninites and derived andesitic-
901 basaltic andesitic glasses.

902 3) If chromite, including microlitic matrix chromite, were to crystallize from these
903 residual liquids, then they would incorporate more Fe^{3+} and Al than observed, as
904 shown by the natural samples taken from the extrusive sequence of the Troodos
905 Ophiolite. Thus, most chromites are products of primitive melt crystallization in the
906 crustal domain or of the incongruent melting of orthopyroxene in the mantle domain.
907 When entrained in an evolving magma, melt oxidation perturbs the equilibrium
908 chromite composition to higher Fe^{3+} . If sufficiently oxidizing conditions are achieved,
909 Fe^{3+} replaces Al efficiently such that $\text{Fe}^{2+}/\text{Fe}^{3+} + \text{Fe}^{3+}/\text{Al}$ chromite-melt equilibrium is
910 approached. The disequilibrium textures and compositions preserved in some
911 phenocrystic-microphenocrystic chromites should be examined closely to ascertain
912 ascent rates using Fe^{3+} diffusivity.

913 4) In chromite, Cr-Al/ Fe^{3+} equilibrium is achieved over much longer timescales. If
914 considered the limiting factor of chromite-melt equilibration, natural
915 microphenocrystic chromite observed in the extrusive suite of the Troodos ophiolite
916 would equilibrate with residual melts in less than *c.* 170 years. Diffusion may be
917 much more rapid, and future work on the diffusive equilibration of both experimental
918 and natural chromites should provide tighter constraints.

919 ACKNOWLEDGEMENTS

920 Thanks go to Mark K. Reagan for providing the natural samples for these experiments, to
921 Michel Pichavant for providing a wealth of insight into interpreting experimental oxygen
922 fugacity data, to Keith Putirka for useful dialogue on opx-melt equilibrium uncertainties, to
923 Fred Davis for insight on chromite equilibria as well as modelling methods, and finally to

924 Alexandre Corgne and an anonymous reviewer for their constructive criticism of this
925 manuscript. This research was funded by the Royal Society of New Zealand through the
926 Marsden Fund (grant MAU1704 to GFZ).

Journal Pre-proofs

927 **REFERENCES**

- 928 Almeev, R.R., Holtz, F., Koepke, J.r., Parat, F. and Botcharnikov, R.E. (2007) The effect of
929 H₂O on olivine crystallization in MORB: Experimental calibration at 200 MPa. *American*
930 *Mineralogist* 92, 670-674.
- 931 Arai, S. (1994) Characterization of spinel peridotites by olivine-spinel compositional
932 relationships: Review and interpretation. *Chemical Geology* 113, 191-204.
- 933 Arai, S. (1997) Origin of podiform chromitites. *Journal of Asian Earth Sciences* 15, 303-310.
- 934 Arai, S. and Yurimoto, H. (1994) Podiform chromitites of the Tari-Misaka ultramafic
935 complex, southwestern Japan, as mantle-melt interaction products. *Economic Geology* 89,
936 1279-1288.
- 937 Arai, S. and Yurimoto, H. (1995) Possible sub-arc origin of podiform chromitites. *Isl. Arc* 4,
938 104-111.
- 939 Arganda-Carreras, I., Kaynig, V., Rueden, C., Eliceiri, K.W., Schindelin, J., Cardona, A. and
940 Sebastian Seung, H. (2017) Trainable Weka Segmentation: a machine learning tool for
941 microscopy pixel classification. *Bioinformatics* 33, 2424-2426.
- 942 Bailey, D.G., Langdon, G.S., Malpas, J. and Robinson, P.T. (1991) Ultramafic and related
943 lavas from the Margi area, Troodos ophiolite, in: Gibson, I.L., Malpas, J., Robinson, P.T.,
944 Xenophontos, C. (Eds.), *Cyprus Crustal Study Project: Initial Report, Holes Cy-1 and 1a*.
945 *Geological Survey of Canada*, pp. 187-202.
- 946 Ballhaus, C. (1998) Origin of podiform chromite deposits by magma mingling. *Earth and*
947 *Planetary Science Letters* 156, 185-193.
- 948 Ballhaus, C., Berry, R.F. and Green, D.H. (1991) High pressure experimental calibration of
949 the olivine-orthopyroxene-spinel oxygen geobarometer: implications for the oxidation state
950 of the upper mantle. *Contributions to Mineralogy and Petrology* 107, 27-40.
- 951 Beattie, P., Ford, C. and Russell, D. (1991) Partition coefficients for olivine-melt and
952 orthopyroxene-melt systems. *Contributions to Mineralogy and Petrology* 109, 212-224.
- 953 Bédard, J.H. (1999) Petrogenesis of Boninites from the Betts Cove Ophiolite, Newfoundland,
954 Canada: Identification of Subducted Source Components. *Journal of Petrology* 40, 1853-
955 1889.
- 956 Birner, S.K., Cottrell, E., Warren, J.M., Kelley, K.A. and Davis, F.A. (2018) Peridotites and
957 basalts reveal broad congruence between two independent records of mantle fO₂ despite local
958 redox heterogeneity. *Earth and Planetary Science Letters* 494, 172-189.
- 959 Bloomer, S.H. and Hawkins, J.W. (1987) Petrology and geochemistry of boninite series
960 volcanic rocks from the Mariana trench. *Contributions to Mineralogy and Petrology* 97, 361-
961 377.
- 962 Blundy, J. and Cashman, K. (2005) Rapid decompression-driven crystallization recorded by
963 melt inclusions from Mount St. Helens volcano. *Geology* 33, 793-796.

- 964 Brandon, A.D. and Draper, D.S. (1996) Constraints on the origin of the oxidation state of
965 mantle overlying subduction zones: An example from Simcoe, Washington, USA.
966 *Geochimica et Cosmochimica Acta* 60, 1739-1749.
- 967 Brounce, M., Reagan, M.K., Coulthard Jr., D.A., Kelley, K.A. and Cottrell, E. (2019) The
968 oxidation states of iron and volatile compositions of Expedition 352 glasses, Goldschmidt
969 2019, Barcelona, Spain.
- 970 Burnham, C.W. (1979) The importance of volatile constituents, in: Yoder, H.S., Jr. (Ed.), *The*
971 *evolution of the igneous rocks*. Princeton University Press, Princeton, New Jersey, pp. 439-
972 482.
- 973 Cameron, W.E. (1985) Petrology and origin of primitive lavas from the Troodos ophiolite,
974 Cyprus. *Contributions to Mineralogy and Petrology* 89, 239-255.
- 975 Cashman, K. and Blundy, J. (2000) Degassing and crystallization of ascending andesite and
976 dacite. *Philosophical Transactions of the Royal Society of London. Series A: Mathematical,*
977 *Physical and Engineering Sciences* 358, 1487-1513.
- 978 Chou, I.M., Eugster, H.P., Berens, P. and Weare, J.H. (1978) Diffusion of hydrogen through
979 platinum membranes at high pressures and temperatures. *Geochimica et Cosmochimica Acta*
980 42, 281-288.
- 981 Cottrell, E., Birner, S., Brounce, M., Davis, F.A., Waters, L.E. and Kelley, K.A. (2020)
982 Oxygen Fugacity Across Tectonic Settings, in: Neuville, D.R., Moretti, R. (Eds.), *AGU*
983 *Geophysical Monograph Redox variables and mechanisms in magmatism and volcanism*.
984 Wiley.
- 985 Couch, S., Sparks, R.S.J. and Carroll, M.R. (2001) Mineral disequilibrium in lavas explained
986 by convective self-mixing in open magma chambers. *Nature* 411, 1037-1039.
- 987 Coulthard Jr, D.A., Reagan, M.K., Shimizu, K., Bindeman, I.N., Brounce, M., Almeev, R.R.,
988 Ryan, J., Chapman, T., Shervais, J. and Pearce, J.A. (2021) Magma Source Evolution
989 Following Subduction Initiation: Evidence From the Element Concentrations, Stable Isotope
990 Ratios, and Water Contents of Volcanic Glasses From the Bonin Forearc (IODP Expedition
991 352). *Geochemistry, Geophysics, Geosystems* 22, doi: [10.1029/2020GC009054](https://doi.org/10.1029/2020GC009054).
- 992 Crank, J. (1975) *The Mathematics of Diffusion*. Oxford University Press, London.
- 993 Dare, S.A.S., Pearce, J.A., McDonald, I. and Styles, M.T. (2009) Tectonic discrimination of
994 peridotites using fO_2 -Cr# and Ga-Ti-Fe^{III} systematics in chrome-spinel. *Chemical Geology*
995 261, 199-216.
- 996 Davis, F.A. and Cottrell, E. (2018) Experimental investigation of basalt and peridotite
997 oxybarometers: Implications for spinel thermodynamic models and Fe³⁺ compatibility during
998 generation of upper mantle melts. *American Mineralogist* 103, 1056-1067.
- 999 Dilek, Y. and Thy, P. (2009) Island arc tholeiite to boninitic melt evolution of the Cretaceous
1000 Kizildag (Turkey) ophiolite: Model for multi-stage early arc-forearc magmatism in Tethyan
1001 subduction factories. *Lithos* 113, 68-87.

- 1002 Droop, G.T.R. (1987) A general equation for estimating Fe³⁺ concentrations in
1003 ferromagnesian silicates and oxides from microprobe analyses, using stoichiometric criteria.
1004 Mineralogical Magazine 51, 431-435.
- 1005 Edwards, S.J., Pearce, J.A. and Freeman, J. (2000) New insights concerning the influence of
1006 water during the formation of podiform chromitite. Geological Society of America Special
1007 Papers 349, 139-148.
- 1008 Evans, K.A., Elburg, M.A. and Kamenetsky, V.S. (2012) Oxidation state of subarc mantle.
1009 Geology 40, 783-786.
- 1010 Falloon, T.J., Malahoff, A., Zonenshaina, L.P. and Bogdanova, Y. (1992) Petrology and
1011 geochemistry of back-arc basin basalts from Lau Basin spreading ridges at 15°, 18° and 19°S.
1012 Mineralogy and Petrology 47, 1-35.
- 1013 Ferracutti, G.R., Gargiulo, M.F., Ganuza, M.L., Bjerg, E.A. and Castro, S.M. (2015)
1014 Determination of the spinel group end-members based on electron microprobe analyses.
1015 Mineralogy and Petrology 109, 153-160.
- 1016 Fisk, M.R. (1986) Basalt magma interaction with harzburgite and the formation of high-
1017 magnesium andesites. Geophysical Research Letters 13, 467-470.
- 1018 Flower, M.F.J. and Levine, H.M. (1987) Petrogenesis of a tholeiite-boninite sequence from
1019 Ayios Mamas, Troodos ophiolite: evidence for splitting of a volcanic arc? Contributions to
1020 Mineralogy and Petrology 97, 509-524.
- 1021 Ford, C., Russell, D., Craven, J. and Fisk, M. (1983) Olivine-liquid equilibria: temperature,
1022 pressure and composition dependence of the crystal/liquid cation partition coefficients for
1023 Mg, Fe²⁺, Ca and Mn. Journal of Petrology 24, 256-266.
- 1024 Frost, B.R. (1991) Introduction to oxygen fugacity and its petrologic importance. Reviews in
1025 Mineralogy and Geochemistry 25, 1-9.
- 1026 Gass, I.G. (1968) Is the Troodos Massif of Cyprus a Fragment of Mesozoic Ocean Floor?
1027 Nature 220, 39-42.
- 1028 Gervilla, F., Asta, M.P., Fanlo, I., Grolimund, D., Ferreira-Sánchez, D., Samson, V.A.,
1029 Hunziker, D., Colas, V., González-Jiménez, J.M., Kerestedjian, T.N. and Sergeeva, I. (2019)
1030 Diffusion pathways of Fe²⁺ and Fe³⁺ during the formation of ferrian chromite: a μ XANES
1031 study. Contributions to Mineralogy and Petrology 174, 65.
- 1032 Ghiorso, M.S. and Sack, R.O. (1995) Chemical mass transfer in magmatic processes IV. A
1033 revised and internally consistent thermodynamic model for the interpolation and
1034 extrapolation of liquid-solid equilibria in magmatic systems at elevated temperatures and
1035 pressures. Contributions to Mineralogy and Petrology 119, 197-212.
- 1036 Golowin, R., Portnyagin, M., Hoernle, K., Sobolev, A., Kuzmin, D. and Werner, R. (2017)
1037 The role and conditions of second-stage mantle melting in the generation of low-Ti tholeiites
1038 and boninites: the case of the Manihiki Plateau and the Troodos ophiolite. Contributions to
1039 Mineralogy and Petrology 172, 104.

- 1040 Gualda, G.A., Ghiorso, M.S., Lemons, R.V. and Carley, T.L. (2012) Rhyolite-MELTS: a
1041 modified calibration of MELTS optimized for silica-rich, fluid-bearing magmatic systems.
1042 *Journal of Petrology* 53, 875-890.
- 1043 Hanson, B. and Jones, J.H. (1998) The systematics of Cr³⁺ and Cr²⁺ partitioning between
1044 olivine and liquid in the presence of spinel. *American Mineralogist* 83, 669-684.
- 1045 Hodel, F., Macouin, M., Trindade, R.I.F., Araujo, J.F.D.F., Respaud, M., Meunier, J.F.,
1046 Cassayre, L., Rouse, S., Drigo, L. and Schorne-Pinto, J. (2020) Magnetic Properties of
1047 Ferritchromite and Cr-Magnetite and Monitoring of Cr-Spinels Alteration in Ultramafic and
1048 Mafic Rocks. *Geochemistry, Geophysics, Geosystems* 21, doi: [10.1029/2020GC009227](https://doi.org/10.1029/2020GC009227).
- 1049 Irvine, T.N. (1967) Chromian spinel as a petrogenetic indicator. Part 2. Petrologic
1050 applications. *Canadian Journal of Earth Sciences* 4, 71-103.
- 1051 Ishikawa, T., Nagaishi, K. and Umino, S. (2002) Boninitic volcanism in the Oman ophiolite:
1052 Implications for thermal condition during transition from spreading ridge to arc. *Geology* 30,
1053 899-902.
- 1054 Jarosewich, E., Nelen, J.A. and Norberg, J.A. (1980) Reference Samples for Electron
1055 Microprobe Analysis*. *Geostandards Newsletter* 4, 43-47.
- 1056 Jégo, S., Pichavant, M. and Mavrogenes, J.A. (2010) Controls on gold solubility in arc
1057 magmas: An experimental study at 1000 C and 4 kbar. *Geochimica et Cosmochimica Acta*
1058 74, 2165-2189.
- 1059 Jochum, K.P., Stoll, B., Herwig, K., Willbold, M., Hofmann, A.W., Amini, M., Aarburg, S.,
1060 Abouchami, W., Hellebrand, E., Mocek, B., Raczek, I., Stracke, A., Alard, O., Bouman, C.,
1061 Becker, S., Dücking, M., Brätz, H., Klemm, R., de Bruin, D., Canil, D., Cornell, D., de Hoog,
1062 C.-J., Dalpé, C., Danyushevsky, L., Eisenhauer, A., Gao, Y., Snow, J.E., Groschopf, N.,
1063 Günther, D., Latkoczy, C., Guillong, M., Hauri, E.H., Höfer, H.E., Lahaye, Y., Horz, K.,
1064 Jacob, D.E., Kasemann, S.A., Kent, A.J.R., Ludwig, T., Zack, T., Mason, P.R.D., Meixner,
1065 A., Rosner, M., Misawa, K., Nash, B.P., Pfänder, J., Premo, W.R., Sun, W.D., Tiepolo, M.,
1066 Vannucci, R., Vennemann, T., Wayne, D. and Woodhead, J.D. (2006) MPI-DING reference
1067 glasses for in situ microanalysis: New reference values for element concentrations and
1068 isotope ratios. *Geochemistry, Geophysics, Geosystems* 7.
- 1069 Jochum, K.P., Willbold, M., Raczek, I., Stoll, B. and Herwig, K. (2005) Chemical
1070 Characterisation of the USGS Reference Glasses GSA-1G, GSC-1G, GSD-1G, GSE-1G,
1071 BCR-2G, BHVO-2G and BIR-1G Using EPMA, ID-TIMS, ID-ICP-MS and LA-ICP-MS.
1072 *Geostandards and Geoanalytical Research* 29, 285-302.
- 1073 Kamenetsky, V.S., Crawford, A.J. and Meffre, S. (2001) Factors controlling chemistry of
1074 magmatic spinel: An empirical study of associated olivine, Cr-spinel and melt inclusions
1075 from primitive rocks. *Journal of Petrology* 42, 655-671.
- 1076 Kamenetsky, V.S., Sobolev, A.V., Eggins, S.M., Crawford, A.J. and Arculus, R.J. (2002)
1077 Olivine-enriched melt inclusions in chromites from low-Ca boninites, Cape Vogel, Papua
1078 New Guinea: evidence for ultramafic primary magma, refractory mantle source and enriched
1079 components. *Chemical Geology* 183, 287-303.

- 1080 Kelley, K.A. and Cottrell, E. (2009) Water and the Oxidation State of Subduction Zone
1081 Magmas. *Science* 325, 605-607.
- 1082 Kelley, K.A. and Cottrell, E. (2012) The influence of magmatic differentiation on the
1083 oxidation state of Fe in a basaltic arc magma. *Earth and Planetary Science Letters* 329-330,
1084 109-121.
- 1085 Klügel, A. (2001) Prolonged reactions between harzburgite xenoliths and silica-
1086 undersaturated melt: implications for dissolution and Fe-Mg interdiffusion rates of
1087 orthopyroxene. *Contributions to Mineralogy and Petrology* 141, 1-14.
- 1088 Kress, V.C. and Carmichael, I.S.E. (1991) The compressibility of silicate liquids containing
1089 Fe₂O₃ and the effect of composition, temperature, oxygen fugacity and pressure on their
1090 redox states. *Contributions to Mineralogy and Petrology* 108, 82-92.
- 1091 La Spina, G., Burton, M., de' Michieli Vitturi, M. and Arzilli, F. (2016) Role of syn-eruptive
1092 plagioclase disequilibrium crystallization in basaltic magma ascent dynamics. *Nature*
1093 *Communications* 7, 13402.
- 1094 Liermann, H.-P. and Ganguly, J. (2002) Diffusion kinetics of Fe²⁺ and Mg in aluminous
1095 spinel: experimental determination and applications. *Geochimica et Cosmochimica Acta* 66,
1096 2903-2913.
- 1097 Liermann, H.P. and Ganguly, J. (2003) Fe²⁺-Mg fractionation between orthopyroxene and
1098 spinel: experimental calibration in the system FeO-MgO-Al₂O₃-Cr₂O₃-SiO₂, and
1099 applications. *Contributions to Mineralogy and Petrology* 145, 217-227.
- 1100 Lloyd, A.S., Ferriss, E., Ruprecht, P., Hauri, E.H., Jicha, B.R. and Plank, T. (2016) An
1101 Assessment of Clinopyroxene as a Recorder of Magmatic Water and Magma Ascent Rate.
1102 *Journal of Petrology* 57, 1865-1885.
- 1103 Lormand, C., Zellmer, G.F., Kilgour, G.N., Németh, K., Palmer, A.S., Sakamoto, N.,
1104 Yurimoto, H., Kuritani, T., Iizuka, Y. and Moebis, A. (2020) Slow ascent of unusually hot
1105 intermediate magmas triggering Strombolian to sub-Plinian eruptions. *Journal of Petrology*.
- 1106 MacLeod, C.J. (1988) The tectonic evolution of the Eastern Limassol Forest Complex,
1107 Cyprus, Department of Earth Sciences. The Open University.
- 1108 Malpas, J. and Langdon, G. (1984) Petrology of the Upper Pillow Lava suite, Troodos
1109 ophiolite, Cyprus. Geological Society, London, Special Publications 13, 155-167.
- 1110 Mattioli, M., Renzulli, A., Menna, M. and Holm, P.M. (2006) Rapid ascent and
1111 contamination of magmas through the thick crust of the CVZ (Andes, Ollagüe region):
1112 Evidence from a nearly aphyric high-K andesite with skeletal olivines. *Journal of*
1113 *Volcanology and Geothermal Research* 158, 87-105.
- 1114 Matveev, S. and Ballhaus, C. (2002) Role of water in the origin of podiform chromitite
1115 deposits. *Earth and Planetary Science Letters* 203, 235-243.
- 1116 Maurel, C. and Maurel, P. (1982) Étude expérimentale de l'équilibre Fe²⁺-Fe³⁺ dans les
1117 spinelles chromifères et les liquides silicatés basiques coexistants, à 1 atm. *Comptes Rendus*
1118 *des Séances de l'Académie des Sciences* 295.

- 1119 Meffre, S., Aitchison, J.C. and Crawford, A.J. (1996) Geochemical evolution and tectonic
1120 significance of boninites and tholeiites from the Koh ophiolite, New Caledonia. *Tectonics* 15,
1121 67-83.
- 1122 Meijer, A. (1980) Primitive arc volcanism and a boninite series: examples from western
1123 Pacific island arcs, in: Hayes, D.E. (Ed.), *The Tectonic and Geologic Evolution of Southeast*
1124 *Asian Seas and Islands*. American Geophysical Union, pp. 269-282.
- 1125 Metcalf, R.V. and Shervais, J.W. (2008) Suprasubduction-zone ophiolites: Is there really an
1126 ophiolite conundrum? *Special Papers-Geological Society of America* 438, 191.
- 1127 Mitchell, A.L. and Grove, T.L. (2016) Experiments on melt–rock reaction in the shallow
1128 mantle wedge. *Contributions to Mineralogy and Petrology* 171, 107.
- 1129 Miyashiro, A. (1973) The Troodos ophiolitic complex was probably formed in an island arc.
1130 *Earth and Planetary Science Letters* 19, 218-224.
- 1131 Moores, E.M., Kellogg, L.H. and Dilek, Y. (2000) Tethyan ophiolites, mantle convection,
1132 and tectonic" historical contingency": A resolution of the" ophiolite conundrum". *Geological*
1133 *Society of America Special Papers* 349, 3-12.
- 1134 Nikolaev, G.S., Ariskin, A.A. and Barmina, G.S. (2018a) SPINMELT-2.0: Simulation of
1135 spinel–melt equilibrium in basaltic systems under pressures up to 15 kbar: I. model
1136 formulation, calibration, and tests. *Geochemistry International* 56, 24-45.
- 1137 Nikolaev, G.S., Ariskin, A.A. and Barmina, G.S. (2018b) SPINMELT-2.0: Simulation of
1138 Spinel–Melt Equilibrium in Basaltic Systems under Pressures up to 15 Kbar: II. Description
1139 of the Program Package, the Topology of the Cr-spinel–Melt Model System, and Petrological
1140 Implications. *Geochemistry International* 56, 125-135.
- 1141 O'Neill, H.S.C., Berry, A.J. and Mallmann, G. (2018) The oxidation state of iron in Mid-
1142 Ocean Ridge Basaltic (MORB) glasses: Implications for their petrogenesis and oxygen
1143 fugacities. *Earth and Planetary Science Letters* 504, 152-162.
- 1144 Ohnenstetter, M., Bechon, F. and Ohnenstetter, D. (1990) Geochemistry and mineralogy of
1145 lavas from the Arakapas Fault Belt, Cyprus: Consequences for magma chamber evolution.
1146 *Mineralogy and Petrology* 41, 105-124.
- 1147 Ozawa, K. (1984) Olivine-spinel geospeedometry: Analysis of diffusion-controlled Mg-Fe²⁺
1148 exchange. *Geochimica et Cosmochimica Acta* 48, 2597-2611.
- 1149 Parkinson, I.J. and Arculus, R.J. (1999) The redox state of subduction zones: insights from
1150 arc-peridotites. *Chemical Geology* 160, 409-423.
- 1151 Pearce, J.A. and Reagan, M.K. (2019) Identification, classification, and interpretation of
1152 boninites from Anthropocene to Eoarchean using Si-Mg-Ti systematics. *Geosphere* 15, 1008-
1153 1037.
- 1154 Pearce, J.A. and Robinson, P.T. (2010) The Troodos ophiolitic complex probably formed in a
1155 subduction initiation, slab edge setting. *Gondwana Research* 18, 60-81.

- 1156 Pownceby, M.I. and O'Neill, H.S.C. (1994) Thermodynamic data from redox reactions at
1157 high temperatures. III. Activity-composition relations in Ni-Pd alloys from EMF
1158 measurements at 850–1250 K, and calibration of the NiO+Ni-Pd assemblage as a redox
1159 sensor. *Contributions to Mineralogy and Petrology* 116, 327-339.
- 1160 Putirka, K.D. (2008) Thermometers and Barometers for Volcanic Systems. *Reviews in*
1161 *Mineralogy and Geochemistry* 69, 61-120.
- 1162 Rautenschlein, M., Jenner, G.A., Hertogen, J., Hofmann, A.W., Kerrich, R., Schmincke, H.U.
1163 and White, W.M. (1985) Isotopic and trace element composition of volcanic glasses from the
1164 Akaki Canyon, Cyprus: implications for the origin of the Troodos ophiolite. *Earth and*
1165 *Planetary Science Letters* 75, 369-383.
- 1166 Reagan, M.K., Ishizuka, O., Stern, R.J., Kelley, K.A., Ohara, Y., Blichert-Toft, J., Bloomer,
1167 S.H., Cash, J., Fryer, P., Hanan, B.B., Hickey-Vargas, R., Ishii, T., Kimura, J.-I., Peate,
1168 D.W., Rowe, M.C. and Woods, M. (2010) Fore-arc basalts and subduction initiation in the
1169 Izu-Bonin-Mariana system. *Geochemistry Geophysics Geosystems* 11.
- 1170 Reagan, M.K. and Meijer, A. (1984) Geology and geochemistry of early arc-volcanic rocks
1171 from Guam. *GSA Bulletin* 95, 701-713.
- 1172 Reagan, M.K., Pearce, J.A., Petronotis, K., Almeev, R.R., Avery, A.J., Carvallo, C.,
1173 Chapman, T., Christeson, G.L., Ferré, E.C., Godard, M., Heaton, D.E., Kirchenbaur, M.,
1174 Kurz, W., Kutterolf, S., Li, H., Li, Y., Michibayashi, K., Morgan, S., Nelson, W.R., Prytulak,
1175 J., Python, M., Robertson, A.H.F., Ryan, J.G., Sager, W.W., Sakuyama, T., Shervais, J.W.,
1176 Shimizu, K. and Whattam, S.A. (2017) Subduction initiation and ophiolite crust: new insights
1177 from IODP drilling. *Int. Geol. Rev.* 59, 1439-1450.
- 1178 Regelous, M., Haase, K.M., Freund, S., Keith, M., Weinzierl, C.G., Beier, C., Brandl, P.A.,
1179 Endres, T. and Schmidt, H. (2014) Formation of the Troodos Ophiolite at a triple junction:
1180 Evidence from trace elements in volcanic glass. *Chemical Geology* 386, 66-79.
- 1181 Robinson, P.T., Melson, W.G., O'Hearn, T. and Schmincke, H.-U. (1983) Volcanic glass
1182 compositions of the Troodos ophiolite, Cyprus. *Geology* 11, 400-404.
- 1183 Roeder, P.L. (1994) Chromite; from the fiery rain of chondrules to the Kilauea Iki lava lake.
1184 *The Canadian Mineralogist* 32, 729-746.
- 1185 Rollinson, H. (2008) The geochemistry of mantle chromitites from the northern part of the
1186 Oman ophiolite: inferred parental melt compositions. *Contributions to Mineralogy and*
1187 *Petrology* 156, 273-288.
- 1188 Rollinson, H., Mameri, L. and Barry, T. (2018) Polymineralic inclusions in mantle
1189 chromitites from the Oman ophiolite indicate a highly magnesian parental melt. *Lithos* 310-
1190 311, 381-391.
- 1191 Scaillet, B., Pichavant, M. and Roux, J. (1995) Experimental crystallization of leucogranite
1192 magmas. *Journal of Petrology* 36, 663-705.
- 1193 Scaillet, B., Pichavant, M., Roux, J., Humbert, G. and Lefevre, A. (1992) Improvements of
1194 the Shaw membrane technique for measurement and control of fH₂ at high temperatures and
1195 pressures. *American Mineralogist* 77, 647-655.

- 1196 Schindelin, J., Arganda-Carreras, I., Frise, E., Kaynig, V., Longair, M., Pietzsch, T.,
1197 Preibisch, S., Rueden, C., Saalfeld, S. and Schmid, B. (2012) Fiji: an open-source platform
1198 for biological-image analysis. *Nature methods* 9, 676.
- 1199 Schmincke, H.-U., Rautenschlein, M., Robinson, P.T. and Mehegan, J.M. (1983) Troodos
1200 extrusive series of Cyprus: A comparison with oceanic crust. *Geology* 11, 405-409.
- 1201 Schouten, H. and Kelemen, P.B. (2002) Melt viscosity, temperature and transport processes,
1202 Troodos ophiolite, Cyprus. *Earth and Planetary Science Letters* 201, 337-352.
- 1203 Scowen, P.A.H., Roeder, P.L. and Helz, R.T. (1991) Reequilibration of chromite within
1204 Kilauea Iki lava lake, Hawaii. *Contributions to Mineralogy and Petrology* 107, 8-20.
- 1205 Shaw, H.R. (1963) Hydrogen-Water Vapor Mixtures: Control of Hydrothermal Atmospheres
1206 by Hydrogen Osmosis. *Science* 139, 1220-1222.
- 1207 Shorttle, O., Moussallam, Y., Hartley, M.E., Maclennan, J., Edmonds, M. and Murton, B.J.
1208 (2015) Fe-XANES analyses of Reykjanes Ridge basalts: Implications for oceanic crust's role
1209 in the solid Earth oxygen cycle. *Earth and Planetary Science Letters* 427, 272-285.
- 1210 Sisson, T.W. and Grove, T.L. (1993) Temperatures and H₂O contents of low-MgO high-
1211 alumina basalts. *Contributions to Mineralogy and Petrology* 113, 167-184.
- 1212 Smith, P.M. and Asimow, P.D. (2005) *Adiabat_1ph*: A new public front-end to the MELTS,
1213 pMELTS, and pHMELTS models. *Geochemistry, Geophysics, Geosystems* 6.
- 1214 Sobolev, A., Portnyagin, M., Dmitriev, L., Tsameryan, O., Danyushevsky, L., Kononkova,
1215 N., Shimizu, N. and Robinson, P. (1993) Petrology of ultramafic lavas and associated rocks
1216 of the Troodos massif, Cyprus. *Petrology* 1, 331-361.
- 1217 Stern, R.J. and Bloomer, S.H. (1992) Subduction zone infancy: Examples from the Eocene
1218 Izu-Bonin-Mariana and Jurassic California arcs. *GSA Bulletin* 104, 1621-1636.
- 1219 Suzuki, A.M., Yasuda, A. and Ozawa, K. (2008) Cr and Al diffusion in chromite spinel:
1220 experimental determination and its implication for diffusion creep. *Phys. Chem. Miner.* 35,
1221 433.
- 1222 Tatsumi, Y. (1981) Melting experiments on a high-magnesian andesite. *Earth and Planetary
1223 Science Letters* 54, 357-365.
- 1224 Tatsumi, Y. (2006) High-Mg Andesites in the Setouchi Volcanic Belt, Southwestern Japan:
1225 Analogy to Archean Magmatism and Continental Crust Formation? *Annual Review of Earth
1226 and Planetary Sciences* 34, 467-499.
- 1227 Taylor, J.R., Wall, V.J. and Pownceby, M.I. (1992) The calibration and application of
1228 accurate redox sensors. *American Mineralogist* 77, 284-295.
- 1229 Thy, P. and Xenophontos, C. (1991) Crystallization Orders and Phase Chemistry of Glassy
1230 Lavas from the Pillow Sequences, Troodos Ophiolite, Cyprus. *Journal of Petrology* 32, 403-
1231 428.

- 1232 Tomiya, A., Miyagi, I., Saito, G. and Geshi, N. (2013) Short time scales of magma-mixing
1233 processes prior to the 2011 eruption of Shinmoedake volcano, Kirishima volcanic group,
1234 Japan. *Bulletin of Volcanology* 75, 750.
- 1235 Ubide, T., Galé, C., Larrea, P., Arranz, E. and Lago, M. (2014) Antecrysts and their effect on
1236 rock compositions: The Cretaceous lamprophyre suite in the Catalonian Coastal Ranges (NE
1237 Spain). *Lithos* 206-207, 214-233.
- 1238 Umino, S. (1986) Magma mixing in boninite sequence of Chichijima, Bonin Islands. *Journal*
1239 *of Volcanology and Geothermal Research* 29, 125-157.
- 1240 Umino, S., Kanayama, K., Kitamura, K., Tamura, A., Ishizuka, O., Senda, R. and Arai, S.
1241 (2018) Did boninite originate from the heterogeneous mantle with recycled ancient slab? *Isl.*
1242 *Arc* 27, e12221.
- 1243 Umino, S., Kitamura, K., Kanayama, K., Tamura, A., Sakamoto, N., Ishizuka, O. and Arai, S.
1244 (2015) Thermal and chemical evolution of the subarc mantle revealed by spinel-hosted melt
1245 inclusions in boninite from the Ogasawara (Bonin) Archipelago, Japan. *Geology* 43, 151-154.
- 1246 Umino, S. and Kushiro, I. (1989) Experimental studies on boninite petrogenesis, in:
1247 Crawford, A.J. (Ed.), *Boninites: And Related Rocks*. Unwin and Hyman, London, pp. 89-
1248 111.
- 1249 Van Orman, J.A. and Crispin, K.L. (2010) Diffusion in Oxides. *Reviews in Mineralogy and*
1250 *Geochemistry* 72, 757-825.
- 1251 Vogt, K., Dohmen, R. and Chakraborty, S. (2015) Fe-Mg diffusion in spinel: New
1252 experimental data and a point defect model†. *American Mineralogist* 100, 2112-2122.
- 1253 Whattam, S.A., Shervais, J.W., Reagan, M.K., Coulthard Jr., D.A., Pearce, J.A., Jones, P.,
1254 Seo, J., Putirka, K., Chapman, T., Heaton, D., Li, H., Nelson, W.R., Shimizu, K. and Stern,
1255 R.J. (2020) Mineral compositions and thermobarometry of basalts and boninites recovered
1256 during IODP Expedition 352 to the Bonin forearc. *American Mineralogist*.
- 1257 Woelki, D., Michael, P., Regelous, M. and Haase, K. (2020) Enrichment of H₂O and fluid-
1258 soluble trace elements in the Troodos Ophiolite: Evidence for a near-trench origin. *Lithos*
1259 356-357, 105299.
- 1260 Woelki, D., Regelous, M., Haase, K.M., Romer, R.H.W. and Beier, C. (2018) Petrogenesis of
1261 boninitic lavas from the Troodos Ophiolite, and comparison with Izu–Bonin–Mariana fore-
1262 arc crust. *Earth and Planetary Science Letters* 498, 203-214.
- 1263 Wolf, K.J. and Eichelberger, J.C. (1997) Syneruptive mixing, degassing, and crystallization
1264 at Redoubt Volcano, eruption of December, 1989 to May 1990. *Journal of Volcanology and*
1265 *Geothermal Research* 75, 19-37.
- 1266 Yajima, K. and Fujimaki, H. (2001) High-Ca and low-Ca boninites from Chichijima, Bonin
1267 (Ogasawara) archipelago. *Japanese Magazine of Mineralogical and Petrological Sciences* 30,
1268 217-236.
- 1269 Zellmer, G.F., Sakamoto, N., Hwang, S.-L., Matsuda, N., Iizuka, Y., Moebis, A. and
1270 Yurimoto, H. (2016) Inferring the Effects of Compositional Boundary Layers on Crystal

- 1271 Nucleation, Growth Textures, and Mineral Chemistry in Natural Volcanic Tephra through
1272 Submicron-Resolution Imaging. *Frontiers in Earth Science* 4.
- 1273 Zellmer, G.F., Sakamoto, N., Iizuka, Y., Miyoshi, M., Tamura, Y., Hsieh, H.-H. and
1274 Yurimoto, H. (2014) Crystal uptake into aphyric arc melts: insights from two-pyroxene
1275 pseudo-decompression paths, plagioclase hygrometry, and measurement of hydrogen in
1276 olivines from mafic volcanics of SW Japan. *Geological Society, London, Special
1277 Publications* 385, SP385. 383.
- 1278 Zhang, Y., Xu, Z., Zhu, M. and Wang, H. (2007) Silicate melt properties and volcanic
1279 eruptions. *Reviews of Geophysics* 45.
- 1280 Zhou, M.-F. and Robinson, P.T. (1997) Origin and tectonic environment of podiform
1281 chromite deposits. *Economic Geology* 92, 259-262.
- 1282 Zhou, M.F., Robinson, P.T. and Bai, W.J. (1994) Formation of podiform chromitites by
1283 melt/rock interaction in the upper mantle. *Mineralium Deposita* 29, 98-101.
- 1284 Zhou, M.F., Robinson, P.T., Malpas, J. and Li, Z. (1996) Podiform chromitites in the
1285 Luobusa ophiolite (Southern Tibet): Implications for melt-rock interaction and chromite
1286 segregation in the upper mantle. *Journal of Petrology* 37, 3-21.
1287

1288 **Figure Captions**

1289 **Figure 1:** A) BSE image of Bon1150U. This image is representative of the “general” texture
1290 observed in the boninitic charges. This includes several examples of euhedral prismatic opx
1291 (dark mineral grains) and platy elongated opx (same colour) set in a relatively homogeneous
1292 glass with anhedral chromite (bright grains). The black orb-shaped parts are vapour bubbles.
1293 B) Close up of an opx cut parallel to the (010) plane exhibiting a ghost core (red ellipse). The
1294 core is likely related to crystallization occurring within the melt/glass phase before stable
1295 thermal conditions were achieved within the IHPV. The arrow points to bright caps that form
1296 at the apices of most if not all opx in this sample (from experiment Bon1200B). These caps
1297 are thought to have grown during quench. The glass adjacent to these minerals is darker,
1298 indicating the loss of iron to the quench-grown rim. C) Broad view of sample Bon1100U with
1299 calcic pyroxene highlighted (red ellipses). Several opx are aligned here, with their c-axes sub-
1300 perpendicular to the image plane. D) BSE image of chromite in Bon1150B after thresholding
1301 brightness and contrast to isolate and amplify Fe enrichment textures.

1302 **Figure 2:** Cation proportion (O = 6) vs Mg# (calculated using Fe_{total}) for opx core analyses.
1303 Literature data are taken from sources listed in the text. Point uncertainties are within the
1304 boundaries of the symbol.

1305 **Figure 3:** Chromite compositional data. A) A portion of a conventional ternary diagram
1306 illustrating the relative proportions of octahedrally coordinated trivalent cations after
1307 recalculation (dimensions of the ternary are illustrated on the inset). Literature data are taken
1308 from sources listed in the text. B) Diagram that illustrates Fe incorporation into both
1309 octahedral and tetrahedral sites using Mg# and the $Fe^{3+}/(Fe^{3+}+Al+Cr)$ parameter. Symbols
1310 same as Figure 2. Analytical uncertainties associated with each composition lie within the
1311 symbol boundaries.

1312 **Figure 4:** A) Equilibrium exchange coefficients calculated for opx and residual melt. B)
1313 Equilibrium exchange coefficients for opx and chromite. Symbols as in Figure 2.

1314 **Figure 5:** Results from MELTS and SPINMELT-2.0 modelling compared to experimental
1315 data (the edge of the ternary diagram from Figure 3A is shown as a dashed line). Lines are
1316 drawn in the direction of decreasing temperature from 1200°C to 1100°C. Solid symbols
1317 represent model data that do not account for iron loss, while empty symbols represent data
1318 generated using models with 30% imposed iron loss.

1319 **Figure 6:** Comparison between average chromite $\text{Fe}^{2+}/\text{Fe}^{3+}$ observed in experimental charges
1320 and modelled equilibrium glass values of the same ratio (grey lines). For equilibrium
1321 conditions to be met, the symbols for each sample would need to lie below the grey lines.

1322 **Figure 7:** Graphical representation of the chemical evolution of chromites within the
1323 compositional space of the spinel prism (inset). Hypothesized relationship: Fe-Mg
1324 interdiffusivity > Fe-Al interdiffusivity > Cr-(Al, Fe) interdiffusivity. If Fe-Mg and Fe-Al
1325 equilibrate chromite $\text{Mg}^\#$, $\text{Fe}^{2+}/\text{Fe}^{3+}$, and Fe^{3+}/Al , with Cr equilibration following, then re-
1326 equilibration is a process that may be approximated by reactions 1 and 2 in a multi-step
1327 fashion. A) Reaction 1 displaces chromite compositions to higher Fe^{2+}/Mg and Fe^{3+}/Al as the
1328 spinel (*s.s.*) component in chromite decreases. In ternary space, this reaction causes a shift to
1329 higher Fe^{3+} concentrations along lines of equal Cr proportion (B). Reaction 2 proceeds along
1330 lines of equal Fe^{3+}/Al (dashed grey line in B) as Cr is lost to the melt phase. Reaction 2
1331 proceeds in a direction perpendicular to the page (up) in A.

1332 **Figure 8:** Partial ternary diagrams (see inset) generated to compare trivalent cation
1333 proportions of natural chromite minerals from the Troodos ophiolite (green triangles) with
1334 modelled chromite compositions generated using SPINMELT-2.0. The grey-bordered green
1335 area underlying the green triangles on the Kalavassos Mine section represents the

1336 compositional range of olivine-hosted chromite inclusions taken from Golowin et al. (2017)
1337 and MacLeod (1988).

1338 **Figure 9:** Diagram summarizing the petrogenetic model wherein disequilibrium textures are
1339 preserved in phenocrystic-microphenocrystic chromite as a function of differences between
1340 the diffusivities of the major divalent and trivalent cations in chromite. A) Spinel octahedron.
1341 Subsequent images use a cross section of this hypothetical mineral form. B) A schematic of
1342 the initial condition of chromite in primitive boninite melt without a large proportion of
1343 silicate minerals. C) Silicate mineral nuclei form, immediately depleting the surrounding melt
1344 in Fe^{2+} and Mg. D) Silicate minerals grow and completely alter the surrounding melt. The
1345 melt has acquired an evolved residual composition rich in Fe^{3+} . E) Hypothetical diffusion
1346 trends for all major cations in chromite from a-a' (transect shown in D).

Table 1: Starting material compositions

	<i>High-Si Boninite</i> *YK0612 974-R6	<i>Troodos Chromitite</i> **Chromite Seed	<i>Boninite Glass</i> **BO-G	<i>Normalized Mixture Composition</i> BO-G with 2 wt% added Chromite
SiO ₂	56.74	0.05	57.92	55.51
TiO ₂	0.17	0.05	0.04	0.17
Cr ₂ O ₃	***0.19	53.81	0.19	1.26
Al ₂ O ₃	10.66	15.11	10.69	10.73
FeO	8.75	15.34	8.38	8.87
MnO	0.23	0.24	0.16	0.23
MgO	15.04	14.01	14.62	15.01
CaO	5.54	-	6.16	5.42
Na ₂ O	2.01	-	1.86	1.97
K ₂ O	0.82	-	0.46	0.80
P ₂ O ₅	0.03	-	0.08	0.03
Total	100.18	98.72	100.48	100.00

*Composition from Reagan et al. (2010, XRF Analysis)

**All analyses of starting materials are provided in the supplemental Tables S1 and S2

***Converted from ppm Cr to wt% Cr₂O₃

- = not quantified

Table 2: Sample identification and characterization, experiment descriptions, and preliminary results

Capsule ID	IHPV Lab	Initial Composition		Experimental Conditions			
		Seed Size (μm)	wt% D ₂ O (1 σ)	T ($^{\circ}\text{C}$)	P (kbar)	pH ₂ ^{added} (bars)	Duration (hrs)
Bon1200Ua	ISTO	x < 32	1.136 (0.142)	1200	2.13	0.0	4.0
Bon1200Ub	ISTO	160 < x < 250	1.395 (0.155)	1200	2.13	0.0	4.0
Bon1200Ba	ISTO	x < 32	0.916 (0.153)	1200	2.12	1.9	1.4
Bon1200Bb	ISTO	160 < x < 250	0.763 (0.191)	1200	2.12	1.9	1.4
Bon1150U	ISTO	x < 32	0.770 (0.128)	1150	2.16	0.0	4.2
Bon1150B	ISTO	x < 32	0.705 (0.141)	1150	2.14	1.4	3.2
Bon1100U	GSJ	x < 32	1.280 (0.142)	1100	2.00	0.0	5.1

Names: *U* = intrinsic $f\text{O}_2$, *B* = buffered $f\text{O}_2$, *a* and *b* designate a difference in the seed size of the chromite added

1348

Table 2 (continued)

Capsule ID	Product Phase Proportions (1 σ)			Activity Model		Oxygen Fugacity		
	Orthopyroxene	Chromite	Glass	Final wt% ² H ₂ O (1 σ)	aH ₂ O (1 σ)	Sensor X _{Ni} (1 σ)	log $f\text{O}_2$ (bars)	ΔNNO (1 σ)
Bon1200Ua	0.49 (0.01)	0.02 (0.01)	0.49 (0.02)	2.32 (0.30)	0.34 (0.07)	0.020 (0.004)	-3.69	3.81 (0.17)
Bon1200Ub	0.50 (0.03)	0.02 (0.00)	0.48 (0.03)	2.91 (0.37)	0.48 (0.08)	0.020 (0.004)	-3.39	4.11 (0.17)
Bon1200Ba	0.59 (0.07)	0.01 (0.00)	0.40 (0.07)	2.29 (0.55)	0.31 (0.11)	0.256 (0.003)	-6.77	0.73 (0.26)
Bon1200Bb	0.55 (0.01)	0.01 (0.01)	0.44 (0.01)	1.73 (0.44)	0.22 (0.08)	0.256 (0.003)	-7.07	0.43 (0.27)
Bon1150U	0.40 (0.08)	0.02 (0.00)	0.58 (0.08)	1.33 (0.29)	0.17 (0.07)	0.020 (0.004)	-4.88	3.21 (0.29)
Bon1150B	0.60 (0.06)	0.02 (0.00)	0.38 (0.05)	1.86 (0.44)	0.26 (0.09)	0.194 (0.003)	-7.09	1.00 (0.26)
Bon1100U	0.45 (0.05)	0.01 (0.01)	0.54 (0.05)	2.37 (0.34)	0.32 (0.07)	0.069 (0.009)	-6.21	2.52 (0.16)

Table 3: Representative compositional data of experiment products (average composition)

<i>Sample</i>	<i>Phase</i>	<i>No. Analyses</i>	SiO ₂	TiO ₂	Cr ₂ O ₃	Al ₂ O ₃	FeO	MnO	MgO	CaO	Na ₂ O	K ₂ O	NiO	Total	Mg#	Cr#	*Fe ²⁺ /Fe ³⁺
Bon1200Ua	Glass	6	61.36	0.07	bdl	16.34	5.90	0.10	2.43	6.51	3.08	0.81	-	96.63	-	-	0.77
	Orthopyroxene	15	55.99	bdl	0.69	1.66	6.59	0.20	33.87	1.09	bdl	-	-	100.14	0.90	0.22	-
	Chromite	4	0.27	bdl	48.62	8.49	24.89	0.36	12.57	-	-	-	0.10	95.36	0.47	0.79	1.17
Bon1200Ub	Glass	8	60.57	0.20	bdl	15.98	7.51	0.14	2.79	6.11	2.52	0.69	-	96.52	-	-	0.76
	Orthopyroxene	13	56.35	bdl	0.67	1.49	6.09	0.18	34.30	0.93	bdl	-	-	100.04	0.91	0.23	-
Bon1200Ba	Glass	5	62.08	0.18	bdl	17.90	5.24	0.13	1.64	6.13	2.99	0.84	-	97.17	-	-	3.35
	Orthopyroxene	13	56.34	bdl	0.71	1.88	7.31	0.20	32.68	1.32	0.05	-	-	100.50	0.89	0.22	-
Bon1200Bb	Glass	2	60.95	0.18	bdl	18.14	5.13	0.14	1.11	6.16	2.92	0.84	-	95.56	-	-	3.84
	Orthopyroxene	9	54.99	bdl	0.68	1.56	7.18	0.20	32.28	1.20	0.15	-	-	98.25	0.89	0.23	-
	Chromite	4	0.12	0.05	50.66	14.36	16.20	0.29	13.16	-	-	-	0.11	95.02	0.59	0.70	3.48
Bon1150U	Glass	4	58.52	0.06	0.05	14.47	7.04	0.11	6.12	8.13	2.59	0.65	-	97.74	-	-	1.00
	Orthopyroxene	8	55.02	bdl	0.64	2.47	8.46	0.23	31.23	1.69	0.06	-	-	99.84	0.87	0.15	-
	Chromite-Core	4	0.11	0.04	51.17	11.86	21.57	0.39	11.62	-	-	-	0.12	96.95	0.49	0.74	2.44
	Chromite-Rim	3	0.15	bdl	48.96	9.34	26.09	0.38	10.89	-	-	-	0.15	96.07	0.43	0.78	1.61
Bon1150B	Glass	3	60.34	0.08	bdl	16.20	5.21	0.10	4.63	7.01	2.94	0.75	-	97.29	-	-	2.74
	Orthopyroxene	2	54.98	bdl	0.70	2.37	9.04	0.24	31.57	1.89	bdl	-	-	100.83	0.86	0.16	-
	Chromite	1	0.08	0.05	51.93	14.45	19.41	0.35	11.5	-	-	-	0.10	97.93	0.51	0.71	4.51
Bon1100U	Glass	5	58.96	0.18	0.14	14.75	6.11	0.13	5.97	8.18	2.59	0.68	-	97.71	-	-	1.31
	Orthopyroxene	3	55.20	0.05	0.44	3.33	9.13	0.29	30.01	2.67	0.10	-	-	101.24	0.85	0.08	-
	Chromite	6	0.07	0.14	50.93	14.41	22.28	0.32	10.96	-	-	-	0.09	99.42	0.47	0.70	3.50

*Calculated using either stoichiometric recalculation (after Droop, 1987) for chromite or the model of Kress and Carmichael (1991) for glass

bdl = below detection limit, - = not analyzed/calculated

Table 4: Predicted and observed equilibrium compositional data for orthopyroxene (opx) and chromite (chrm)

<u>Modelled</u>	<u>$K_D(Fe-Mg)^{opx-liq} (1\sigma)$</u>	<u>$*K_D(Fe-Mg)^{chrm-opx}$</u>
Bon1200Ua	0.209 (0.007)	4.594
Bon1200Ub	0.211 (0.003)	-
Bon1200Ba	0.201 (0.005)	-
Bon1200Bb	0.199 (0.002)	4.639
Bon1150U	0.233 (0.001)	4.936
Bon1150B	0.219 (0.003)	4.957
Bon1100U	0.231 (0.009)	5.098
<u>Observed</u>		
Bon1200Ua	0.080 (0.004)	5.475 (0.260)
Bon1200Ub	0.066 (0.003)	-
Bon1200Ba	0.070 (0.005)	-
Bon1200Bb	0.048 (0.001)	4.279 (0.110)
Bon1150U	0.236 (0.011)	5.103 (0.237)
Bon1150B	0.246 (0.013)	4.863 (0.238)
Bon1100U	0.298 (0.010)	5.194 (0.171)

1 σ is a quantification of the distribution of modelled/observed values based on analytical precision and detected heterogeneity

**Model uncertainty = $c. \pm 0.157 (1\sigma)$ using error propagation*

Table 5: Assessment of Fe-Mg equilibrium between opx, chromite, and melt in Kapilio lavas

<i>Opx data (norm.)</i>	SiO ₂	Al ₂ O ₃	FeO	MnO	MgO	CaO	<i>Moles MgO</i>	<i>Moles FeO</i>	X_{Al}^{opx}
*AM-4 opx-a	55.38	2.71	9.01	0.00	32.43	0.47	0.805	0.125	0.112
*AM-4 opx-b	56.14	1.65	8.15	0.00	32.63	1.43	0.810	0.113	0.068
<i>Chromite data</i>	Cr ₂ O ₃	Al ₂ O ₃	FeO	MgO	Total				<i>Average Y_{Cr}^{chrom}</i>
*AM-4 chrm-a	51.65	9.82	23.73	9.59	94.79		0.238	0.244	0.70
*AM-4 chrm-b	52.71	9.98	23.43	11.60	97.72		0.288	0.216	
*AM-4 chrm-c	53.80	10.18	23.46	11.25	98.69		0.279	0.228	
<i>Glass data and model K_D</i>	<i>**Average Model $K_D(Fe-Mg)^{opx-liq}$ (1σ)</i>			<i>**Average melt molar MgO (1σ)</i>			<i>**Average melt molar FeO (1σ)</i>		
	0.292 (0.004)			0.232 (0.024)			0.108 (0.004)		
<i>Modelled $K_D(Fe-Mg)^{chrom-opx}$</i>	opx-a	opx-b	<i>***(1σ)</i>						
1030°C (0.5 kbar)	4.676	4.955	0.157						
1130°C (0.5 kbar)	5.408	5.755	^						
	* Taken from Flower and Levine (1987)								
	** Compiled from all available analyses of Kapilio glass from Woelki et al. (2020)								
<i>Observed K_D Values</i>	$K_D(Fe-Mg)$	<i>***(1σ)</i>		<i>Equilibrium?</i>			<i>*** Same model uncertainty as in previous table</i>		
opx-a and average melt	0.334	0.041		yes			**** Calculated using error propagation methods applied to average melt composition		
opx-b and average melt	0.300	^		yes			^ = Same as above		
chrm-a and opx-a	6.587	-		no			- = Cannot be calculated using available data		
chrm-a and opx-b	7.324	-		no					
chrm-b and opx-a	4.827	-		yes (1030°C)					
chrm-b and opx-b	5.367	-		yes (mod T)					
chrm-c and opx-a	5.238	-		yes (mod T)					
chrm-c and opx-b	5.824	-		yes (opx-b 1130°C)					

Table 6: Ascent time calculations

<i>Chromite Radius (μm)</i>	<i>Maximum Ascent Time from Cr-Al Diffusion (years)</i>		<i>Minimum Ascent Time from Fe-Mg Diffusion (days)</i>	
	<i>at 1030 °C</i>	<i>at 1130 °C</i>	<i>at 1030 °C</i>	<i>at 1130 °C</i>
15	43	2	56	15
20	77	4	99	27
25	120	6	155	42
30	173	8	223	60
<i>log D (cm^2/sec)</i>	-16.2	-14.9	-12.7	-12.2

Declaration of interests

The authors declare that they have no known competing financial interests or personal relationships that could have appeared to influence the work reported in this paper.

The authors declare the following financial interests/personal relationships which may be considered as potential competing interests: